ADVANCED MATERIALS INTERFACES
Open Access
www.advmatinterfaces.de

Prelithiated Carbon Nanotube-Embedded Silicon-based Negative Electrodes for High-Energy Density Lithium-Ion Batteries

Leyla Ünal, Viviane Maccio-Figgemeier, Lukas Haneke, Gebrekidan Gebresilassie Eshetu,* Johannes Kasnatscheew, Martin Winter, and Egbert Figgemeier**

Multi-walled carbon Nanotubes (MWCNTs) are hailed as beneficial conductive agents in Silicon (Si)-based negative electrodes due to their unique features enlisting high electronic conductivity and the ability to offer additional space for accommodating the massive volume expansion of Si during (de-)lithiation. However, both MWCNTs and Siirreversibly consume an enormous amount of Li inventory to principally form a Solid Electrolyte Interphase (SEI) and due to other parasitic reactions, which results in lowering the Coulombic Efficiency (CE), rapid decrease in reversible capacity, and shorter battery life.To tackle these hurdles, electrochemical prelithiation is adopted as a taming strategy to mitigate the large capacity loss (nearly reducing the first irreversible capacity by ≈60%) of MWCNT-Si/Graphite (Gr) negative electrode-based full-cells. In contrast, a yardstick negative electrode utilizing commercially used Super P (Super P-Si/Gr) showed a reduction of ≈47% after in vitro pre-doping with lithium, which is considerably smaller compared to that of MWCNTs-based electrode design. Furthermore, the Initial CE, life cycle, and rate capability are enhanced by prelithiation. Interestingly, prelithiation brings more impact on MWCNTs -Si/Gr than with Super P-Si/Gr design. An in-depth analysis using X-ray photoelectron spectroscopy (XPS), RAMAN Spectroscopy, Attenuated Total Reflection Fourier Transform Infrared Spectroscopy (ATR FTIR), laser microscopy, and Scanning Electron Microscopy (SEM) reveal deeper insights into the differences in SEI layer between prelithiated MWCNTs and their Super P-based electrode counterparts.

1. Introduction

Lithium-ion batteries (LIBs) revolutionized our lives since they first entered the market in 1991 by Sony.[1] Due to their low self-discharge rate, low maintenance, free of memory effort, high energy density and long cycle lifespan, they play an important role in various applications including in consumer electronics (laptops, telephones, camcorders etc.), electrification of land and air transport, sustainable integration of renewable energy sources (e.g., solar and wind), and utility/smart grid storage.[2] Currently, Graphite (Gr) presents to be industry-standard negative electrode material in LIBs owing to its structural stability and low volume changes (≤ 10%) during charge–discharge process, suitable operating potential (≤ 0.2 V vs. Li/Li^+) and reasonable ionic and electronic conductivity.[3] However, Gr provides a theoretical specific capacity of 372 mAh g^{-1} (LiC_6),[1,4] which is inept for enabling next-generation applications such as the large-scale deployment of electric vehicles and thus to meet the demand for long-driving range

L. Ünal, E. Figgemeier
Helmholtz Institute Münster (HI MS)
IEK-12
Forschungszentrum Jülich GmbH
Campus Boulevard 89, 52074 Aachen, Germany
E-mail: l.uenal@fz-juelich.de; e.figgemeier@fz-juelich.de

The ORCID identification number(s) for the author(s) of this article can be found under https://doi.org/10.1002/admi.202400024

DOI: 10.1002/admi.202400024

V. Maccio-Figgemeier, G. G. Eshetu, E. Figgemeier
Center for Ageing
Reliability and Lifetime Prediction of Electrochemical and Power Electronic Systems (CARL)
RWTH Aachen University
Campus Boulevard 89, 52074 Aachen, Germany
E-mail: gebrekidan.eshetu@isea.rwth-aachen.de

L. Haneke, J. Kasnatscheew, M. Winter
Insitute of Physical Chemistry
MEET Battery Research Center University of Münster
48149 Münster, Germany

G. G. Eshetu
Department of Material Science and Engineering
Mekelle Institute of Technology, Mekelle University
1632, Tigray Ethiopia

and fast-charging LiBs.[2,5] This calls for the exploration of novel chemistries and materials that provide high-energy density, and thus evade the "driving range anxiety".[2,6]

Among Li-alloy forming materials, Silicon (Si) is undoubtedly the most auspicious negative electrode candidate to realize high-energy density LIBs. This is due to its various enticing features such as high theoretical specific capacity of 3590 mAh g^{-1} (for $Li_{3.75}Si$ phase at 20 °C, which is nearly 10 times greater than that of Gr), high natural abundance in the earth's crust and thus competitive price, environmental friendliness[7] and suitable operating potential window (< 0.5 V vs. Li/Li^+).[2,8] However, the commercialization of Si negative electrode–based LiBs is not yet realized because of various unavoidable intrinsic challenges such as large eolotropic volume change (≥ 300%)[9] during cell operation, resulting in mechanical stress followed by crack formation and degradation of the negative electrode; low electronic and ionic conductivity ($\delta_{e^-} \approx 10^{-3}$ S cm^{-1} and $D_{Li+} \approx 10^{-14}$–10^{-13} m^2 s^{-1}), and fragile SEI layer.[2,10] The large volume changes can lead to the continuous formation and decomposition of the SEI layer, which is accompanied by the consumption of a large amount of Li-inventory, making the SEI layer thicker and inhomogeneous. This results in an unstable interphase, electrolyte drying out and high impedance.[11] As a result, the loss of electronic contact among active particles and from the current collector occurs, leading to a decline in obtainable capacity and reduced cycling stability.[2,6,12]

Substantial efforts have been devoted to address these problems and their undelying mechanisms including the use of designer electrolyte additives, electrode conductive additives, polymeric binders, electrode design, co-utilization of Si and Gr via bledning or composite design, etc.[2,6] Recently, Carbon Nanotubes (CNTs) have been considered as an ideal conductive additive in Si-based negative electrodes due to their high electronic conductivity and ability to accommodate the large volume change associated with Si. In literature, it has been assumed that Si particles are tightly wrapped by CNTs conductive network, buffering its large volume changes during (de-)lithiation, and thus eliminating the drawbacks of Si.[8,13] Furthermore, the highly conductive network can enhance the overall electronic conductivity of Si-based negative electrode systems, resulting in improved cycling and power output and longer lifespan of the battery cells.[13,14] However, the large surface area of CNTs and high surface reactivity of Si contribute to active Li inventory consumption during the initial and subsequent cycles. As a result, the combination of Si with CNTs leads to a significant irreversible capacity, causing a decrease in the Initial Coulombic Efficiency (ICE) and ensuing long-term cycling. The large initial capacity losses should be minimized as they directly impact the energy density of the battery cell.[15] In this regard, prelithiation, which involves introducing extra active Li into negative electrodes prior to cell assembly (in vitro), can be regarded as a promising approach to compensate the initial capacity losses and pre-form tunable SEI layer, and thus enhance the ICE and long-term cycling stability of MWCNTs-containing Si-negative electrodes-based full-cells.[7] This innovative approach has the potential to offer a range of advantages, such as a high energy density, extended lifespan, and hence circumventing intrinsic challenges linked with thermodynamically unstable electrochemical systems.[16]

The main objective of the present study is reducing the initial irreversible capacity of MWCNTs-Si/Gr negative electrode-based full-cells through an in vitro electrochemical prelithiation. For comparison and pre-doping induced impact assessment, Si/Gr utilzing commercially available Super P additive is employed. Results of electrochemical cycling test of full-cells constructed from prelithiated MWCNTs-Si/Gr and Super P-Si/Gr -based negative and NMC622 positive electrodes demonstrate that the initial irreversible capacity in MWCNTs-Si/Gr negative electrodes-based full-cells can be effectively mitigated (reduced by ≈60%) through the in vitro electrochemical prelithiation. However, such pre-doping is found to be less effective in Super P-Si/Gr negative electrode-based full-cells (reduced by ≈47%). In addition, pre-doping with Li is found to improve the reversible capacity of MWCNTs-Si/Gr negative electrodes-based full-cells from 101.4 ± 5.0 mAh g^{-1} to 129.3 ± 5.3 mAh g^{-1} at 100th cycle, whereas for Super P-Si/Gr electrode system, only an increase from 101.2 ± 4.8 to 114.2 ± 14.2 mAh g^{-1} could be observed. To understand and elucidate the underlying causes of the differences, a comprehensive examination has been carried out utilizing a range of surface-sensitive techniques such as laser microscopy, Scanning Electron Microscopy (SEM), RAMAN spectroscopy, Attenuated Total Reflection Fourier Transform Infrared Spectroscopy (ATR-FTIR), and X-ray photoelectron spectroscopy (XPS). This study provides a profound insight and understanding of the surface morphology and chemistry of both types of negative electrodes in their pristine, prelithiated, pristine-cycled, and prelithiated-cycled states.

2. Results and Discussion

2.1. Structural and Morphological Characterization

Figure 1 presents the comparative laser microscopy images and picture of the as fabricated MWCNTs-Si/Gr and Super P-Si/Gr negative electrodes. **Table 1** displays the negative electrode's composition, areal mass loading and thickness.

It is evident that different electrode additives result in distinct morphologies and structures of the Si/Gr negative electrodes as observed in the SEM images. For instance, MWCNTs-Si/Gr negative electrode displays inhomogeneously distributed large Si-alloy particles across its entire surface, while Super P-Si/Gr negative electrode either has no or only a few minimally visible large Si-alloy particles (Figure 1a,b). The presence of MWCNTs contributes to the formation of such large Si-alloy particles, which is a well-documented challenge in the dispersion process of MWCNTs as reported in literature.[17] Interestingly, laser microscope images presented in Figure 1b reveal surface cracks on Super P-Si/Gr, which are not visible on MWCNTs-Si/Gr (Figure 1a). In addition, images depicted in Figure 1c demonstrate that Super P-Si/Gr undergoes severe cracking when subjected to bending, whereas MWCNTs-Si/Gr does not display such deformation or cracking. This implies that MWCNTs-Si/Gr exhibits superior mechanical stability and enhanced adhesion to the current collector compared to Super P- Si/Gr, which are critical factors for the efficient battery operation.

The morphological differences between the two negative electrodes have been further elucidated through SEM analysis, as illustrated in **Figure 2**.

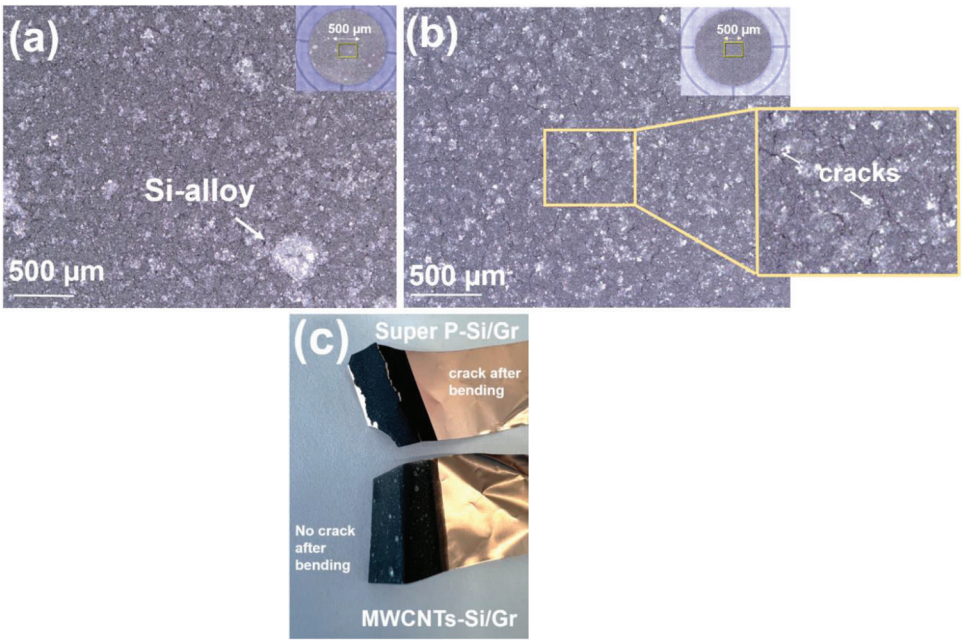

Figure 1. Laser microscopy surface images of: a) MWCNTs-Si/Gr, b) Super P-Si/Gr, and c) pictures of MWCNTs-Si/Gr and Super P-Si/Gr negative electrodes before and after bending test (mechanical stability).

Table 1. Negative electrode recipe and properties.

Negative Electrode	components in wt%					Areal mass loading [mg cm^{-2}]	Electrode thickness [µm]
	Super P	MWCNTs	Si-alloy	Gr	CMC		
MWCNTs-Si/Gr	–	10	60	20	10	4.9	66
Super P-Si/Gr	10	–	60	20	10	4.7	56

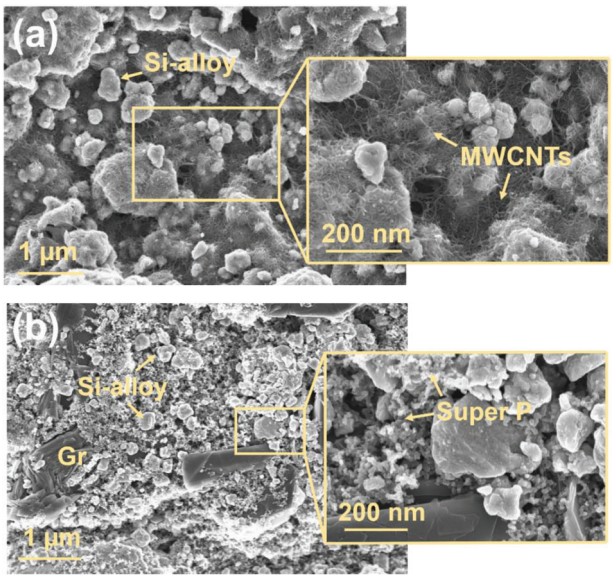

Figure 2. Comparative SEM surface images of pristine: a) MWCNTs-Si/Gr, and b) Super P-Si/Gr negative electrodes.

SEM images clearly show that while Gr particles are entirely covered, Si-alloy particles (size distribution ranging from 0.9 to 24 µm) are found to be encapsulated by the MWCNTs. Moreover, it can be clearly seen that MWCNTs establish networking among the particles by effectively binding them through their thread-like structure (Figure 2a). On the contrary, Super P forms cluster agglomerates which are distributed over the electrode surface, surrounding the active particles (Figure 2b). Nevertheless, Gr and Si particles remain visible in distinct regions, which is not observed in the presence of MWCNTs that entirely cover the active particles (Figure 2a).

2.2. Electrochemical Performance

Aiming at examining the impact of in vitro electrochemical prelithiation on the overall performance of MWCNTs-Si/Gr and Super P-Si/Gr negative electrodes based full-cells, prelithiated and pristine (without prelithiation) negative electrodes were coupled with Ni-rich positive electrode (i.e., $LiNi_{0.6}Mn_{0.2}Co_{0.2}O_2$, NMC622) and cycled at C/2 in a voltage range of 2.8 – 4.35 V up to 200 cycles. **Figure 3** shows key performance metrics of full-cell configurations: a) long-term cycling performance, b) CE, c) initial voltage profiles of pristine and prelithiated MWCNTs-Si/Gr

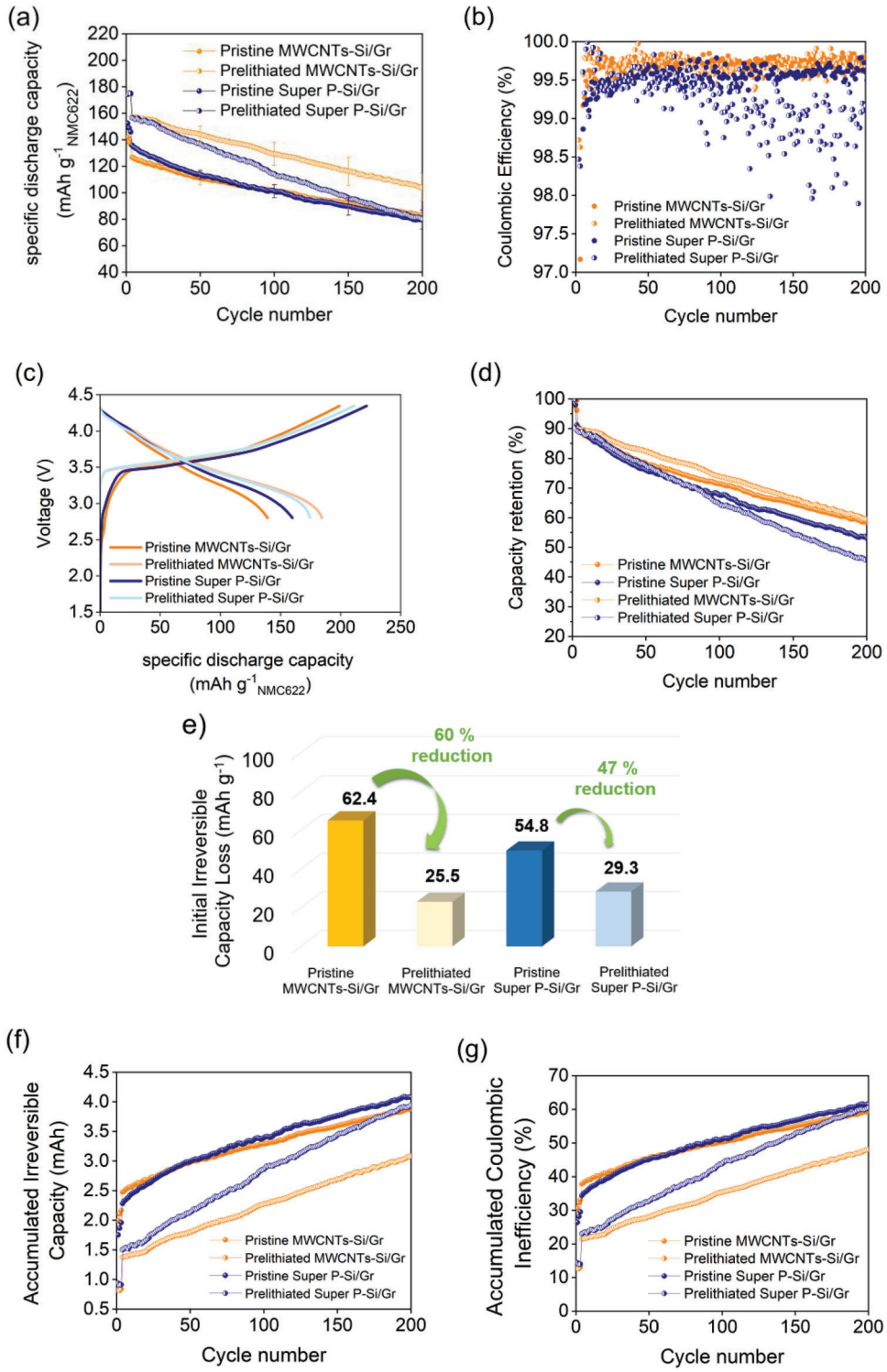

Figure 3. Full-cells: a) long-term cycling performance, b) CE, c) initial voltage profiles, d) capacity retention, e) irreversible capacity obtained from first cycle, f) Accumulated Irreversible Capacity, and g) Accumulated Coulombic Inefficiency.

Table 2. Summary of Electrochemical performance results of pristine and prelithiated MWCNTs-Si/Gr and Super P-Si/Gr negative electrodes-based full-cells.

Negative electrode	ICE [%]	Initial Irreversible capacity [mAh g^{-1}]	Specific discharge capacity at 100th cycle [mAh g^{-1}]	Capacity retention at 100th cycle [%]
Pristine MWCNTs-Si/Gr	69.5	62.4	101.4 ± 5.0	71.5
Prelithiated MWCNTs-Si/Gr	87.2	25.5	129.3 ± 5.3	73.9
Pristine Super P-Si/Gr	73.6	54.8	101.2 ± 4.8	67.9
Prelithiated Super P-Si/Gr	85.6	29.3	114.2 ± 14.2	65.1

and Super P-Si/Gr negative electrode-based full-cells, d) capacity retention, e) irreversible capacity obtained from first cycle of prelithiated and pristine Si/Gr negative electrodes-based full-cells, and f,g) comparative Accumulated Irreversible Capacity and Accumulated Coulombic Inefficiency. **Table 2** provides a comparative overview of the electrochemical performance data.

Without prelithiation, MWCNTs-Si/Gr negative electrode-based battery cell exhibits lower capacity within the first 50 cycles as compared to Super P-Si/Gr negative electrode-based full-cell. This could be due to the formation of an SEI layer and its associated high initial irreversible capacity and low ICE (Figure 3a, Table 2). Interestingly, however, Super P-Si/Gr electrode-based full-cell shows a decreased CE and more rapid capacity decay after 50 cycles compared to the pristine MWCNTs-based full-cell (Figure 3b,d). This can be attributed to the structural stability and tuned SEI layer in MWCNTs-Si/Gr negative electrodes. MWCNT material, known for its high surface area (175 m^2 g^{-1}),[18] naturally possesses functional groups such as electrochemically active residual oxygen, nitrogen, etc., allowing dipole-dipole interactions/hydrogen bonding with the carboxylate groups of the CMC binder, resulting in a strong adhesion. The network formed by MWCNTs and CMC contributes to the overall structural stability and improved mechanical strength, and thus effectively compensating high volume changes experienced by Si, and which in turn ultimately improve the long-term cyclability. On the other hand, Super P, with its lower surface area (62 m^2 g^{-1}) and possibly less reactive surface moieties, does not tend to form strong interactions. This assumption is further supported by the findings in Figure 1c, where no cracks were visible on the MWCNTs-Si/Gr electrode design when subjected to bending, in contrast to the Super P-Si/Gr electrode design which presented cracks.

Adoption of electrochemical prelithiation enhances the overall reversible (obtainable) capacity, rate capability, and cycle life of full-cells constructed from MWCNTs-Si/Gr and Super P-Si/Gr negative electrodes. This is in line with previous report despite a smaller amount (i.e, 2%) and different form of MWCNT (aqueous dispersion instead of powder) was used.[41] Figure 3a,b highlights a significant enhancement in long-term cycling performance and CE for both cell systems in comparison to their pristine states.

Interestingly, prelithiated MWCNTs- Si/Gr negative electrode-based full-cell exhibits enhanced cycling performance and higher CE compared to prelithiated Super P-Si/Gr negative electrode-based full-cell, which almost coincides with the performance of its corresponding pristine state at the end of the 200 cycles (Figure 3a). For instance, cells with prelithiated MWCNTs-Si/Gr electrode- demonstrate a discharge reversible capacity of 129.3 ± 5.3 mAh g^{-1} at 100th cycle, whereas the full-cell with Super P-Si/Gr electrode displays a significantly lower discharge reversible capacity of 114.2 ± 14.2 mAh g^{-1} (Figure 3a, Table 2). These results imply that pre-doping with Li has a huge positive impact on MWCNTs-Si/Gr negative electrode-based full-cells compared to that of Super P-Si/Gr full-cells. This is due to the fact that prelithiation endows MWCNTs-Si/Gr negative electrode with a robust SEI layer which in turn boosts the performance of the corresponding full-cell. It can be also attributed to the high specific surface area of MWCNTs, which promotes more reactivity and facilitates electrolyte reduction during the early stages, leading to the formation of an SEI with an optimized thickness and composition. In contrast, Super P exhibits a lower specific surface area (62 m^2 g^{-1}), leading to lower reactivity on its surface and thereby forming an unstable SEI layer with negative impact during prolonged cycling. This can also be linked to a decline and fluctuating CE until 200th cycle for prelithiated Super P-Si/Gr negative electrode-based full-cells, which is also accompanied by a relatively lower electrochemical performance. Conversely, prelithiated MWCNTs-Si/Gr negative electrode-based full-cell shows no significant decrease in CE, reaching a value of 99.7% after the 200th cycle (Figure 3b). Furthermore, the initial voltage profiles (Figure 3c) clearly demonstrate that the first discharge capacity for the MWCNTs-Si/Gr full-cells is significantly increased by prelithiation compared to its pristine state. Interestingly, this improvement was found to be much higher (improved by 23.3% from 141.8 ± 7.6 to 174.9 ± 8.3 mAh g^{-1}) compared to Super P-Si/Gr full-cell, demonstrating less enhancement in capacity, i.e., 14.3% from 152.5 ± 6.3 to 174.3 ± 4.3 mAh g^{-1}. In addition, prelithiation results in a significant rise in the ICE for the MWCNTs-Si/Gr full-cell configuration as compared to that of Super P-based cell (Table 2). The improved cyclability of pristine and prelithiated MWCNTs-Si/Gr negative electrode-based full-cells is further shown in the enhancement of capacity retention (Figure 3d, Table 2). First, MWCNT additive has a positive impact on the cyclability of Si/Gr-based full-cells, while Super P leads to a faster capacity degradation. In vitro prelithiation negatively affects Super P- Si/Gr electrode-based full-cells, showing much higher capacity degradation compared to its pristine and prelithiated MWCNTs-Si/Gr cell design. Another advantage of prelithiation is that the first irreversible capacity can be mitigated by ≈60% in MWCNTs-Si/Gr electrode-based full-cells, while for the benchmarking cell system, only a reduction of ≈47% can be achieved (Figure 3e, Table 2). These findings demonstrate that in vitro electrochemical prelithiation effectively reduces the first irreversible capacity of full-cells, with augmented impact on MWCNTs-Si/Gr electrodes as compared to Super P-Si/Gr- based systems.

Aiming at obtaining an in-depth insight into the various parasitic reactions and their impacts, Accumulative Irreversible

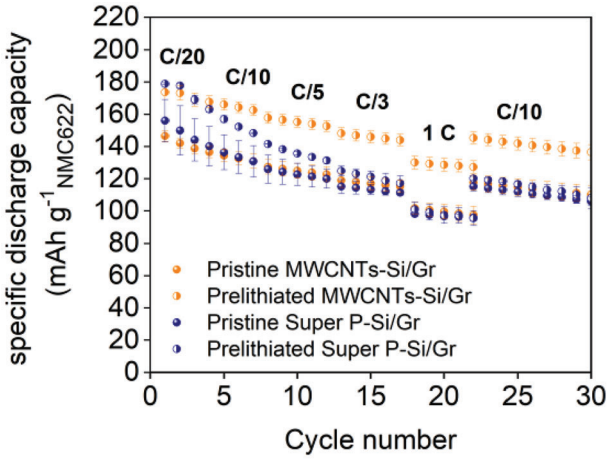

Figure 4. Rate capability of pristine and prelithiated MWCNTs-Si/Gr and Super P-Si/Gr negative electrode-based full-cells.

Capacity (Q_{AIC}) and Accumulative Coulombic Inefficiency (Q_{ACIE}) estimations were employed as finger - of- merit.[19] The irreversible capacity (Q_{irr}, Equation 1) refers to charge loss associated with active lithium loss and parasitic reactions that do not consume lithium, including theformation of SEI layer, diffusion-controlled lithium trapping and plating, electronically disconnected Li, redox shuttle reactions, gas formation from residual water, surface moeties induced and other reactions. On the other hand, Q_{AIC} (Equation 1) represents the sum of irreversible capacity over a certain number (n) of charge–discharge cycles.[19,20] Furthermore, the accumulated Coulombic Inefficiency (Q_{ACIE}) corresponds to the sum of the Coulombic Inefficiencies over a certain number of charge–discharge (Equation 2).

$$Q_{irr} = Q_{charge} - Q_{discharge}, Q_{AIC} = \sum_{1}^{n} Q_{irr}(n)\,[mAh] \quad (1)$$

$$CE = \frac{Q_d}{Q_c} \times 100\%, CIE = 100 - CE[\%], A_{CIE} = \sum_{1}^{n} A_{CIE}(n)\,[\%] \quad (2)$$

Figure 3f,g illustrates Q_{AIC} and Q_{ACIE} for pristine and prelithiated negative electrode-based full-cells. Prelithiated Super P-Si/Gr - based full-cells possess a remarkably increased slope compared to that of prelithiated MWCNTs-Si/Gr-based full-cells, and are in line with the obtained electrochemical performance (Figure 3a,b,d). This difference can be attributed to the formation of an ineffective SEI layer on prelithiated Super P- Si/Gr electrode, which results in higher consumption of Li inventory during cycling due to the large volume changes of Si and disconnection of particles. In contrast, a more robust and effective SEI layer is formed on prelithiated MWCNT-Si/Gr negative electrode that reduces electrolyte degradation and at the same time buffers the anisotropic volume expansion of Si. This finding is further reflected in the Q_{ACIE}, where the slope for the prelithiated Super P-Si/Gr-based fullcell exhibits a drastic increase until 200th cycle compared to that of MWCNTs-based system.

Figure 4 depicts the power ouput of full-cells fabricated from both MWCNTs and Super P - based electrodes in their pristine and prelithiated states at various C-rates (C/10, C/5, C/3, and 1C). Prelithiated MWCNTs-Si/Gr negative electrode-based full-cell shows superior rate capability across all C-rates (while more visible at 1C) compared to its Super P counterpart. Recovery test (cycling back to C/10) also evidences that prelithiated MWCNTs-Si/Gr based full-cell presents much better performance. The amelioration in power output could be attributed to: 1) faster activation, i.e., the battery cell can deliver or accept charge at a faster rate without significant loss of capacity, and 2) enhanced lithium ion mobility through the formation of a highly regulated SEI layer and thus improving the overall ionic conductivity of the battery cell. Despite higher amount (i.e., 10%) and powder form of MWCNTs was employed in this study, similar trends both in terms of long-term cycling and rate capability, were demonstrated previously with 2% MWCNTs, but the MWCNTs was in aqueous dispersion form (not powder).[41]

Further analysis on the impact of in vitro prelithiation is carried out using differential capacity analysis (dQ/dV vs. voltage) of charge-discharge process as shown in **Figure 5**. The differences in peak intensity and positions are linked to intrinsic parasitic reactions or material losses. Considering Ohm's law ($V = I \times R$), widening of the peaks is related to the chemical changes in the electrode material, and shifting in position to a higher voltage range indicates an increase in internal resistance.[21]

After 100th cycle, pristine MWCNTs-Si/Gr electrode-based full-cell exhibits a decrease in peak intensity and a significant widening of the peak, suggesting lower level of electrochemical activity compared to its prelithiated state. Additionally, the peaks observed in the pristine electrodes are shifted toward higher voltage ranges, indicating a higher internal resistance as compared to their prelithiated states, which is evidenced by results of the rate capability. Similar results are obtained for the Si/Gr electrode-based full-cell system with Super P additive. However, the peak after the 100th cycle is more intense for the prelithiated MWCNTs-Si/Gr electrode-based full-cell compared to the prelithiated Super P-based cell. These findings corroborate the positive impact and superior electrochemical performance of prelithiated MWCNTs-Si/Grnegative electrode-based full-cells as demonstrated in Figures 3 and 4.

Briefly, the above electrochemical investigations and obtained results prove that prelithiation has a prodigious beneficial impact on the electrochemical performance of MWCNTs-Si/Gr negative electrode-based full-cells compared to that of prelithiated Super P-Si/Gr negative electrode-based full-cells.

2.3. Post-Mortem Investigation of Prelithiated, Pristine-Cycled and Prelithiated-Cycled Negative Electrodes

2.3.1. Optical and Morphological Analysis

Figure 6 illustrates the comparative laser microscopy images of pristine, prelithiated, pristine-cycled, and prelithiated-cycled states of MWCNTs-Si/Gr and Super P-Si/Gr negative electrodes. After prelithiation, MWCNTs-Si/Gr negative electrode exhibits a slightly golden hue on its surface, indicating a partially lithiated state in the Si/Gr negative electrode (Figure 6c).[22] In contrast, the presence of this golden surface is less or not visible on the prelithiated Super P-Si/Gr negative electrode surface (Figure 6d). After cycling with and without prelithiation, clear differences can

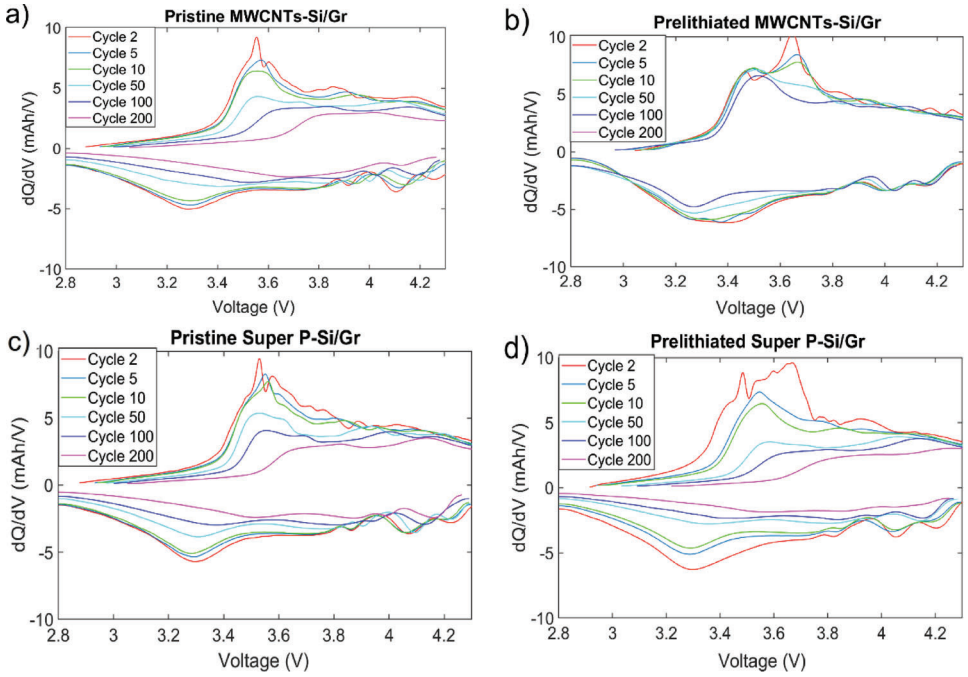

Figure 5. *dQ/dV* versus voltage analysis of pristine and prelithiated MWCNTs-Si/Gr and Super P-Si/Gr negative electrode-based full-cells.

be observed between the negative electrodes. Pristine-cycled Super P-Si/Gr negative electrode is detached from Cu foil, whereas the pristine-cycled MWCNTs-Si/Gr negative electrode displays no cracks or any detachments (Figure 6e,f). Both electrodes exhibit a gold-colored surface, indicating that they were in a lithiated state as mentioned above.[22] Prelithiated-cycled MWCNTs-Si/Gr negative electrode shows a partial detachment from Cu foil and the golden hue is still visible, whereas the Super P-Si/Gr negative electrode is completely detached from the current collector and the golden hue is not present anymore (Figure 6g,h).

As discussed in the section dedicated to the morphological investigation of negative electrodes, the utilization of MWCNTs additive offers an enhanced level of mechanical stability. This is achieved by facilitating stronger inter-particle adhesion as well as adhesion to the current collector. Consequently, the use of MWCNTs effectively prevents any deformation to applied stress that may arise during cycling, primarily caused by the enormous volume expansion of Si. Furthermore, electrochemical analysis evidences, that the presence of large Si-alloy particles on the surface of MWCNT-containing samples does not have any detrimental effects on the electrochemical performance. In order to obtain a more precise and accurate understanding of the morphology of the negative electrodes, SEM images were recorded. **Figure 7** displays SEM images of MWCNTs-Si/Gr and Super P-Si/Gr electrodes in their pristine, prelithiated, pristine-cycled, and prelithiated-cycled states.

MWCNTs, which were previously clearly visible in the pristine state (Figure 7a), are no longer detectable after prelithiation. The MWCNTs are entirely covered by the electrolyte decomposition products (Figure 7c). In their pristine-cycled state, the MWCNTs are not visible and the negative electrode surface is surrounded by an even passivation layer (Figure 7e). Interestingly, the passivation layer on the prelithiated-cycled MWCNTs-Si/Gr negative electrode surface is considerably rougher (Figure 7g), indicating that prelithiation has a significant influence on the formation of the SEI layer. In contrast, Super P in SuperP-Si/Gr is clearly detectable, both in their prelithiated and pristine-cycled states (Figure 7d,f). Moreover, prelithiated-cycled Super P-Si/Gr negative electrode is covered by an uneven surface layer (Figure 7h), suggesting its potential irreversible reaction with electrolyte decomposition products and/or electrolyte salts. The difference in morphology on prelithiated-cycled state supports the assumption of the formation of a more stable passivation layer on MWCNTs-Si/Gr electrodes, which is rather a smooth one (Figure 7g), whereas Super P-based negative electrode shows irregularities on its passivation layer which may occur due to the SEI layer degradation (Figure 7h).

2.3.2. RAMAN and ATR-FTIR Spectroscopy Analysis

Raman spectroscopy provides insights into the key properties of sp^2 carbons.[23] In general, carbon-based materials exhibit three distinct Raman bands, namely D, G, and 2D. The G-band is ascribed to graphitic structure (sp^2) and corresponds to the in-plane vibration of the C—C bonds within the graphene sheets, while the D-band is associated with structural defects.[24] The 2D band provides information about the number of layers present on the surface of a given carboneous material. It arises from a double resonance-enhanced two-phonon lateral vibrational process.[23] **Figure 8** shows Raman spectra of MWCNTs-Si/Gr and Super P-Si/Gr negative electrodes in their pristine, prelithiated, pristine-cycled, and prelithiated-cycled states.

Raman spectra for pristine Si/Gr negative electrodes display a G-band at ≈1580 cm^{-1}, a D-band at ≈1345 cm^{-1}, and a 2D-band at ≈2692 cm^{-1} (Figure 8). R values are comparable for both

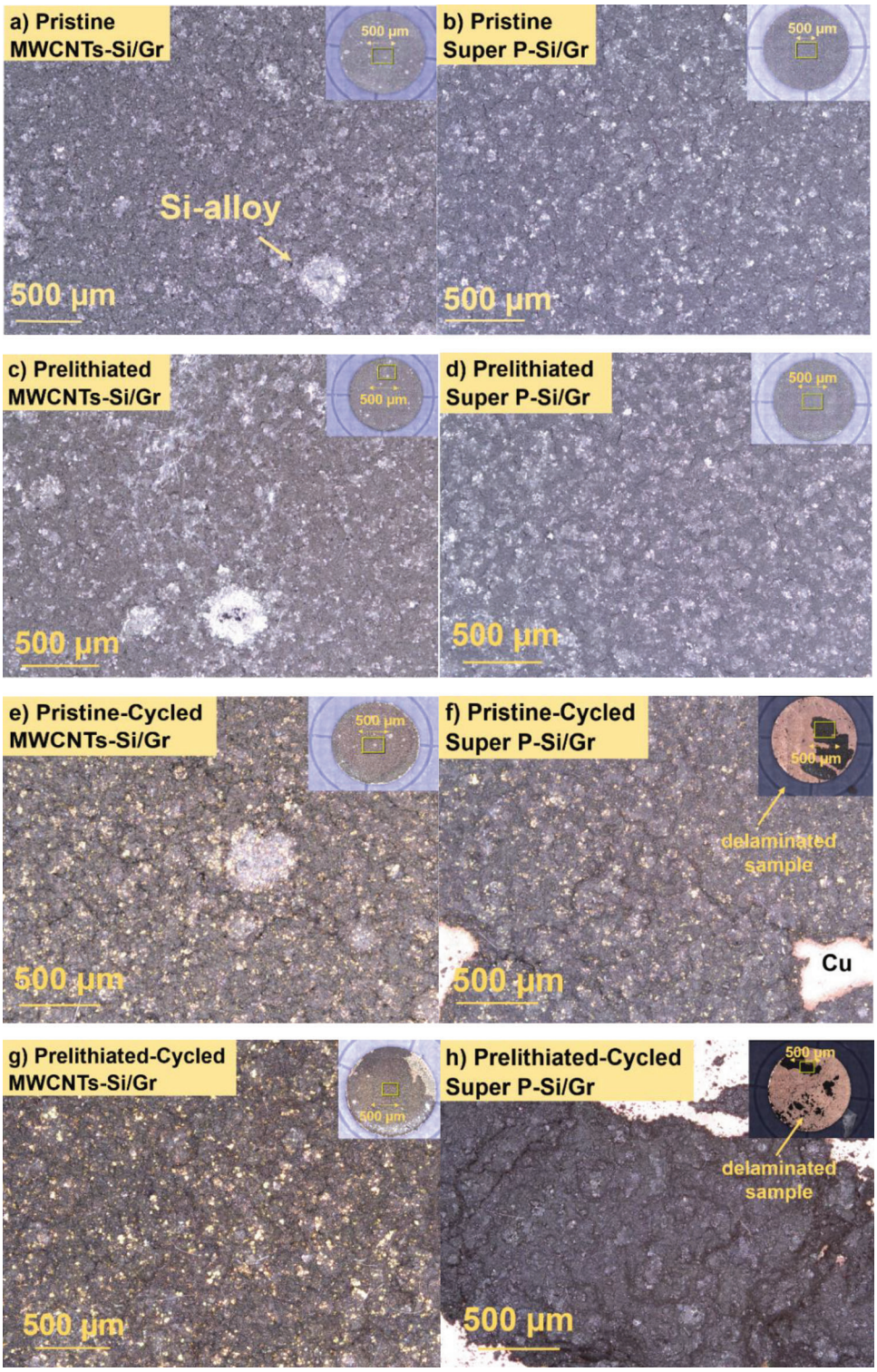

Figure 6. Laser microscopy images of: a,b) pristine MWCNTs-Si/Gr and Super P-Si/Gr, c,d) prelithiated MWCNTs-Si/Gr and Super P-Si/Gr, e,f) pristine-cycled MWCNTs-Si/Gr and Super P-Si/Gr, and g,h) prelithiated-cycled MWCNTs-Si/Gr and Super P-Si/Gr.

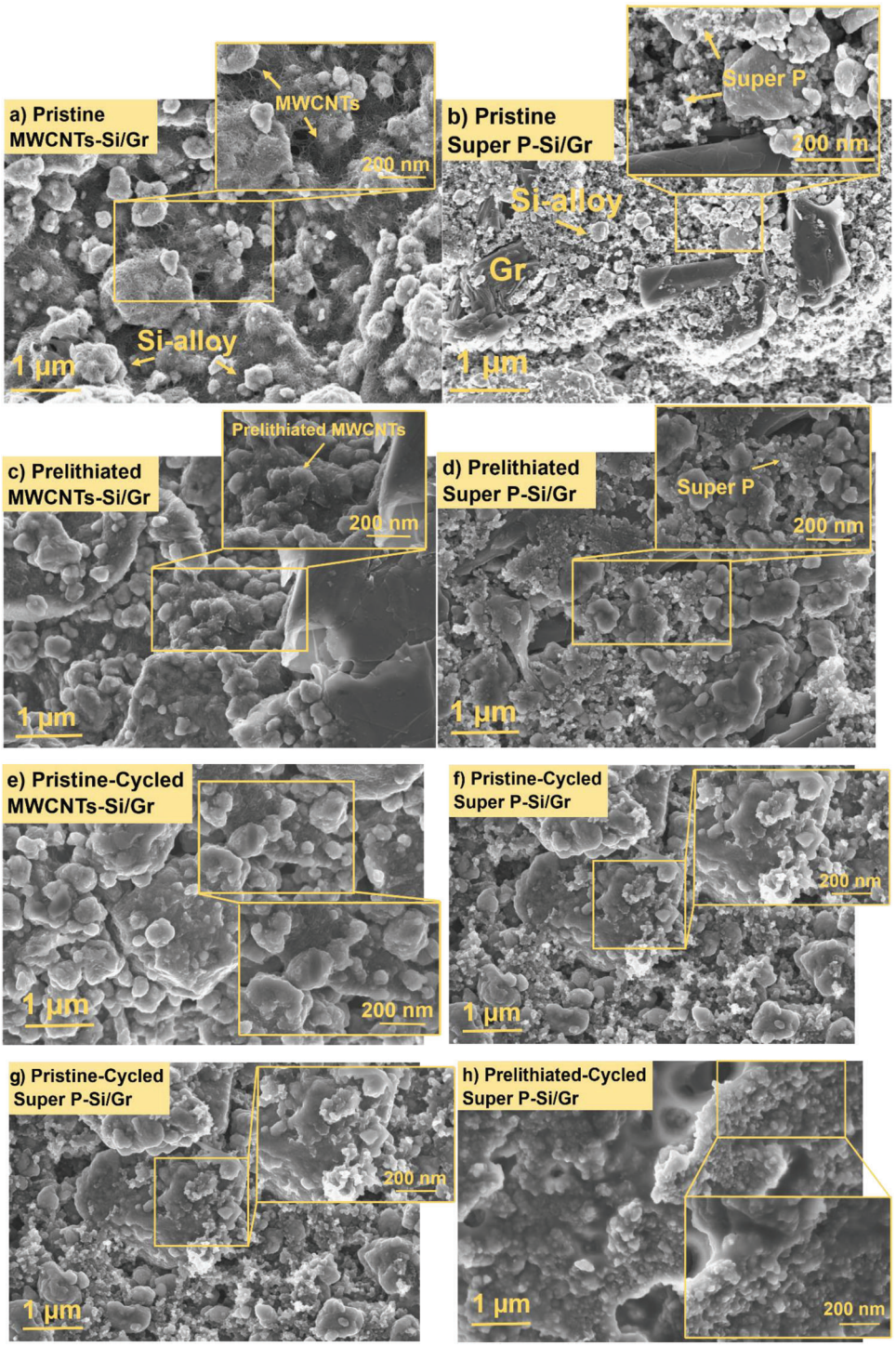

Figure 7. SEM images of a,b) pristine MWCNTs-Si/Gr and Super P-Si/Gr, c,d) prelithiated MWCNTs-Si/Gr and Super P-Si/Gr, e,f) pristine-cycled MWCNTs-Si/Gr and Super P-Si/Gr, g,h) prelithiated-cycled MWCNTs-Si/Gr and Super P-Si/Gr.

negative electrode systems in their pristine states (MWCNTs-Si/Gr ≈1.04 and Super P-Si/Gr ≈1.06). Notably, the 2D-band is conspicuously absent in pristine Super P-Si/Gr negative electrode, whereas it is present in MWCNTs-Si/Gr electrode design, indicating the presence of multiple graphene layers in MWCNTs. Additionally, a pronounced peak at 515 cm^{-1} is evident in the Raman spectrum for the pristine Super P-Si/Gr, which is attributed to the crystalline state of Si (c-Si)[33] but is absent in the MWCNTs-Si/Gr negative electrode spectrum. Additionally, a shoulder peak is observed in the G-band, which is a characteristic

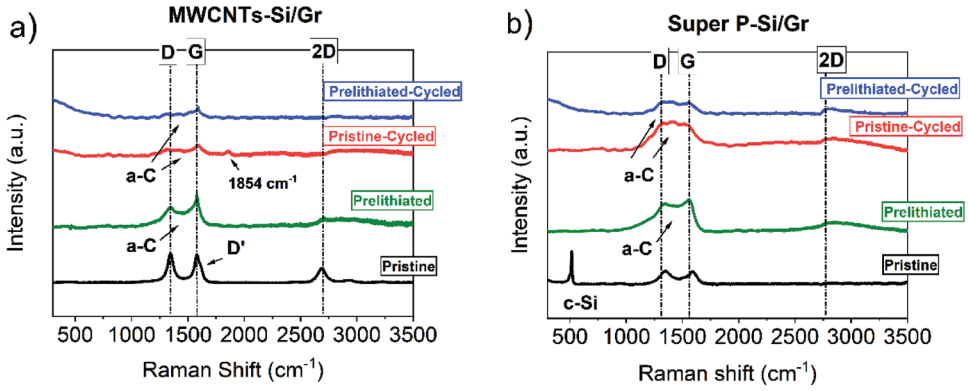

Figure 8. Raman spectra of: a) pristine, prelithiated, pristine-cycled and prelithiated-cycled MWCNTs-Si/Gr negative electrodes, and b) pristine, prelithiated, pristine-cycled and prelithiated-cycled Super P-Si/Gr negative electrodes.

feature of MWCNTs.[23,25] In their prelithiated, pristine-cycled, and prelithiated-cycled states, the D- and G-bands demonstrate a significant broadening and a discernible bump is detected within the 2690–3100 cm^{-1} range for both electrode types. This can be attributed to the presence of amorphous carbon (a-C).[26] The presence of a-C contributes to activation of new multiple peaks that lead to the broadening of the D-and G-bands, as well as to the emergence of the bump within the 2D range.[26,27] Furthermore, the intense c-Si peak in Super P-Si/Gr disappeared due to high degree of amorphization. The upshift in the D-band occurred on prelithiated, pristine-cycled, and prelithiated-cycled negative electrodes can be attributed to the presence of amorphous carbon (a-C).

Interestingly, the G-band for prelithiated, pristine-cycled, and prelithiated-cycled MWCNTs-Si/Gr negative electrode is more intense than for Super P-Si/Gr electrode design, showing that MWCNTs electrode system exhibits more graphitic degree/ordered surface structure after cycling. In the literature, higher graphitic degree is proposed to affect the electrochemical performance, leading to enhanced electrochemical conductivity of electrode materials.[28] Due to the inherent higher electronic conductivity of MWCNTs compared to Super P, G peak observed in cycled negative electrodes is more intense, potentially resulting in enhanced cycling properties as supported by the obtained electrochemical data (Figures 3 and 4). Furthermore, an additional peak at 1854 cm^{-1} is observed in the pristine-cycled MWCNTs-Si/Gr electrode. This new peak has been previously reported in the literature, but its interpretation varies, with some studies suggesting it as an indicator of Li plating or is attributed to Li_2C_2, an SEI layer compound resulting from reactions (Equations 3–5).[29] While Li_2CO_3 and C_2H_4 are the results of two ($2e^-$) and one ($1e^-$) electron reduction of ethylene carbonate (EC), respectively, CO_2 can emanate from the acid-base reactions of the highly basic SEI components (e.g., Li_2CO_3 and $LiROCO_2$) with the unavoidable traces of H_2O and HF.[30] In this study, however, no Li plating is detected through laser images, and since the cells were cycled at a low current (C/10), the most plausible species could be lithium carbide (Li_2C_2).

$$CO_3^{2-} + 5e^- + 7Li^+ \rightarrow 3Li_2O + 1/2Li_2C_2 \quad (3)$$

$$C_2H_4 + 6Li^0 \rightarrow 4LiH + Li_2C_2 \quad (4)$$

$$2CO_2 + 6Li^0 \rightarrow 4Li_2O + Li_2C_2 \quad (5)$$

Another applicable tool used in this study is ATR-FTIR spectroscopy, which has emerged as a reliable method for examining the surface chemistry of electrode materials. It enables the acquisition of comprehensive knowledge regarding the composition of the surface film, both after prelithiation, and cycling (with and without prelithiation procedure). **Figure 9** shows the ATR-FTIR spectrum of pristine, prelithiated, pristine-cycled, and prelithiated-cycled MWCNTs-Si/Gr and Super P-Si/Gr negative electrodes.

ATR-FTIR spectra of pristine-cycled and prelithiated-cycled negative electrodes show peaks at 2800–3000 cm^{-1} (attributed to CH- in ROLi and/or in $ROCO_2Li$), 1760 cm^{-1} (C═O) of ester (RCO_2R'; R = alkyl group) as confirmed by the presence of peaks at 1190 cm^{-1} (C—O—C), 1470–1400 cm^{-1} (—CH_2 in $ROCO_2Li$ or C—O in Li_2CO_3), 1075–1080 cm^{-1} (C—O in $(CH_2COCO_2Li)_2$), 830–720 cm^{-1} (-OCO_2 in $ROCO_2Li$), 540–550 cm^{-1} (Li-O),[31] and the peak at 1650–1620 cm^{-1} (C═O) is due to lithium alkyl carbonate ($ROCO_2Li$).[32] The comparison of pristine-cycled spectra between the two types of negative electrodes exhibits no significant differences both in peak position and intensity.However, the differences become apparent in the prelithiated-cycled states. Specifically, the ATR-FTIR spectrum of prelithiated-cycled Super P-Si/Gr exhibits a peak at 1575 cm^{-1} (C═O) of carboxylate salt RCO^{2-} (such as in CMC), which are evident in both the pristine and prelithiated-cycled states. The presence of these peaks indicates potential degradation of the SEI layer formed on a prelithiated-cycled Super P-Si/Gr negative electrode. This supports the findings obtained from SEM images (Figure 7h) showing a different passivation layer formed on prelithiated-cycled Super P-Si/Gr negative electrode as compared to prelithiated-cycled MWCNTs-Si/Gr electrode. **Table 3** summarizes the observed peaks from pristine, prelithiated, pristine-cycled, and prelithiated-cycled negative electrodes, along with their functional group assignments and corresponding interpretations.

Overall, RAMAN and ATR-FTIR spectroscopy measurements indicate remarkable differences between pristine-cycled and prelithiated-cycled negative electrode surfaces, corroborating the variation evidenced in morphology and electrochemical performance. For an in-depth surface investigation on the nature

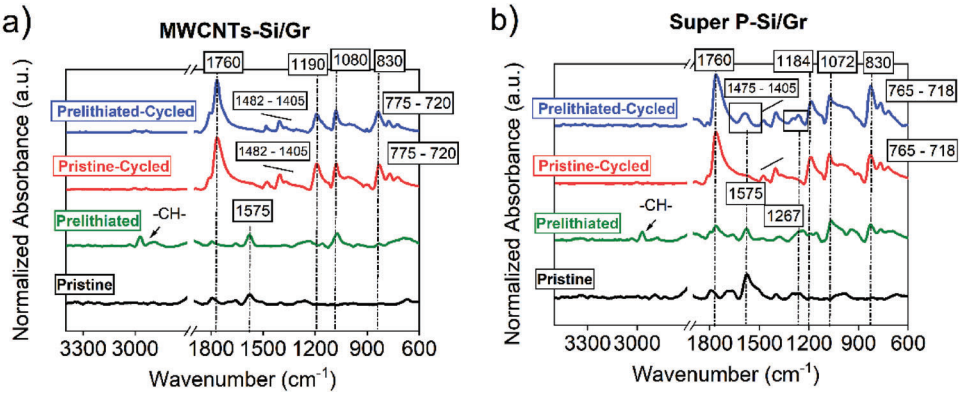

Figure 9. ATR-FTIR spectra of: a) pristine, prelithiated, pristine-cycled and prelithiated-cycled MWCNTs-Si/Gr negative electrodes, and b) pristine, prelithiated, pristine-cycled and prelithiated-cycled Super P-Si/Gr negative electrodes.

of the SEI layer–including chemical makeup, XPS analysis is carried out as presented and thoroughly discussed below.

2.4. Surface Chemistry Characterization by XPS

Herein, XPS analysis was carried out to get an in-depth insight into the nature of SEI layer formed on prelithiated and cycled MWCNTs-Si/Gr and Super P-Si/Gr negative electrodes. This investigation aims to elucidate the surface chemistry of prelithiated, pristine-cycled, and prelithiated-cycled negative electrodes with MWCNTs and Super P as electrode conductive agents. For the sake of clarity and organization, XPS results are discussed in two sets: 1.) organic layer, inorganic composition, and elemental analysis of the prelithiated and on cycled (without prelithiation) Si/Gr negative electrodes, and 2.) Prelithiated-cycled Si/Gr negative electrodes.

Table 3. Summary of ATR-FTIR peaks measured on prelithiated, pristine-cycled, and prelithiated-cycled MWCNTs- Si/Gr and Super P- Si/Gr negative electrodes.

Peak [cm^{-1}]	functional group	Interpretation	References
1763–1766 1190–1200	C═O str.	EC residual	[33]
1656	C═O asm str.		[31b,d]
1477.3, 1404	CH_2 bend		[31b,d]
1305.6	C═O sym str.	$(CH_2COCO_2Li)_2$	[31b]
1080	C—O str.		[31b,d]
835	OCO_2 bend		[31b]
1477.3, 1404	C—O str.		[31d,34]
900, 1470	CO_3^{2-} bend	Li_2CO_3	[31a]
2935	C—H str.		[31a,e]
1080, 1008.6	C—O str.	ROLi	[31a,e]
545.8	Li—O str.		[31e]
2935.3	C—H		[31b,c]
1656	C═O asym str.		[31b,d]
1477.3, 1404	CH_2 bend		[31b,e]
1305.6	C═O sym str.	$ROCO_2Li$	[31b]
1080	C—O str.		[31a]
835.1	CO_3 bend		[31b,c,e]
545.7	Li—O str.	Li_2O	[31a,e]
1570	C═O asym str.	RCO_2Li	[35]

2.4.1. XPS Analysis on Prelithiated and on Cycled (Without Prelithiation) Si/Gr negative Electrodes

Carbonaceous SEI layer Composition: Organic Layer: The layer near the interface with the electrolyte solution is assumed to be both ductile and more porous composed of largely organic components like lithium alkyl carbonates, lithium alkoxides, and ethylene oxide oligomers originating from (electro)chemical decomposition products of EC (Equations 6–10)[31,36] and EMC used in this study. The main electrochemical decomposition pathways of EC reduction and decomposition reactions of the SEI building compounds are shown as follows:

$$2(CH_2O)_2CO + 2Li^+ + 2e^- \rightarrow 2LiOCO_2C_2H_{4(radical)}^{\cdot} \quad (6)$$

$$2LiOCO_2C_2H_{4(radical)}^{\cdot} \rightarrow [LiOCO_2CH_2]_2 + C_2H_4 \uparrow \quad (7)$$

$$[LiOCO_2CH_2]_2 + 2Li^+ + 2e^- \rightarrow 2Li_2CO_3 + C_2H_4 \uparrow \quad (8)$$

$$Li_2CO_3 + 2Li^+ + 2e^- \rightarrow 2Li_2O + CO \uparrow \quad (9)$$

$$(CH_2O)_2CO \rightarrow (-CH_2 - CH_2 - O-)_n \quad (10)$$

The reduction reaction of EC results in the formation of $LiOCO_2C_2H_4$ radical (Reaction (6)) and the resulting $LiOCO_2C_2H_4$ radicals recombine leading to the formation of dilithium ethylene dicarbonate ($[LiOCO_2CH_2]_2$: LiEDC) and a hydrocarbon gas molecule (C_2H_4, Reaction (7)). LiEDC is considered to be a primary component of the SEI layer in EC-based electrolytes.[2] However, it is reported to be more soluble and decomposes into lithium carbonate (Li_2CO_3) and C_2H_4 (Reaction (8)).[37] Li_2CO_3 can further electrochemically decompose to form Li_2O and CO molecules (Reaction (9)). Furthermore, EC can undergo a polymerization reaction (Reaction (10)) forming poly(ethylene oxide), PEO ($-CH_2-CH_2-O-)_n$, through ring-opening in the presence of strong nucleophiles like ROLi and PF_5.[2]

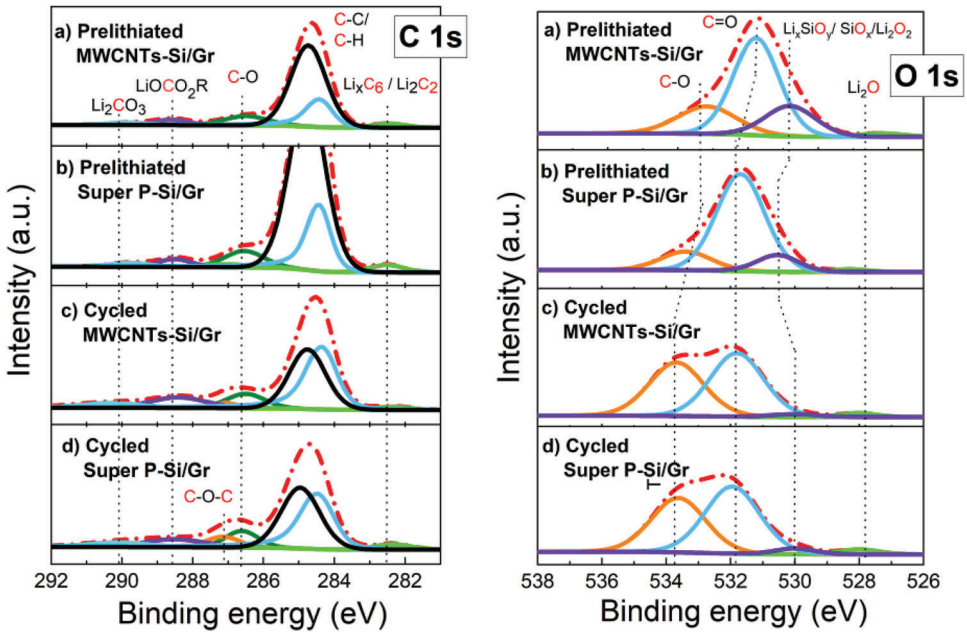

Figure 10. C1 s and O 1 s spectra of: a,b) prelithiated, and c,d) cycled MWCNTs-Si/Gr and Super P-Si/Gr negative electrodes.

C 1s spectra of prelithiated and cycled negative electrodes are shown in **Figure 10**, deconvoluted into seven peaks: Li_xC_6/Li_2C_2 at 282.4 eV, C—C (sp^2) / C—H (sp^3) at 284.6 eV –285.0 eV, C—O at ≈286.5 eV, C—O—C ($-CH_2-CH_2-O-)_n$) at ≈287 eV, and various carbonates such as Li_2CO_3 or organic lithium alkyl carbonates ($ROCO_2Li$), and carboxyl groups (COOR) at 288.5–291 eV.[38] The C—C (sp^2) / C—H (sp^3) peak at 284.6 eV – 284.8 eV can be assigned to Li-free Gr material as well as to conductive agents (MWCNTs and Super P). The lithiated species Li_xC_6/Li_2C_2 (depending on the degree of lithiation) are assumed as bulk reference signal and their detection in higher atomic fraction implies that the SEI formed on prelithiated samples is thinner than on cycled samples.[2] The C 1s peak at 286.5 eV correlates to a carbon atom from carbonyl groups, C—O, resulting from EC ring-opening - induced polymerization and appears to be slightly stronger in prelithiated negative electrodes than in cycled spectra. However, this is not very clear and evident. Interestingly, however, the C—O—C peak is visible on cycled MWCNTs-Si/Gr and Super P-Si/Gr negative electrodes (predominantly on cycled Super P-Si/Gr). This may infer that during prelithiation, low amount of solvent molecules (EC and/or EMC) are reduced and thus resulting in a very low amount of solvent reduction-induced SEI building species like LiEDC $(LiOCO_2CH_2)_2$. Furthermore, the binding energies in the range of 288–291 eV display carboxylate carbon in lithium alkyl carbonates ($ROCO_2Li$) and lithium carbonates (Li_2CO_3), which are decomposition products of EC and are present on both prelithiated as well as cycled negative electrodes.

The O 1s spectrum shows a broad band that can be deconvoluted into two peaks; one at 531.8–532 eV ascribed to oxygen double bonded to carbon (C═O) [as in the case of Li_2CO_3 and $ROCO_2Li$] and the second at 533.8 eV due to oxygen single bonded to carbon (C—O) [$LiOCH_3$ and ethylene oxide-based oligomers (PEO)]. In prelithiated negative electrodes, the C═O signal is strong while the C—O peak is broader and weaker. In contrast, the C—O peak is more intense in the cycled negative electrode compared to prelithiated samples. These are in line with the C 1s spectra that the SEI layer on prelithiated negative electrodes contains relatively more C═O and less C—O-bearing compounds than in the cycled samples.

Inorganic SEI layer Composition: Inorganic Layer: Inorganic components of the SEI layer are mainly decomposition products of electrolyte salt anions (PF_6^- in this study), and are predominantly located in the highly reducing environment near the electrode surface. For EC:EMC/$LiPF_6$ electrolyte, the inorganic SEI building components include Li_2CO_3, Li_2O, LiF, Li_xPF_y, and $Li_xPF_yO_z$ (Reaction equations 11–18). While the organic layer is assumed to be ductile and thermodynamically and kinetically metastable, the inner inorganic layer is dense and stiff, and its constituents are relatively thermodynamically stable and insoluble in the state-of-the-art non-aqueous solvents, thus providing better mechanical stability to the SEI layer.[37] F 1s spectrum in **Figure 11** shows stronger peaks for LiF (685 eV) and electrolyte salt ($LiPF_6$, 687eV), and decomposition products of $LiPF_6$ on cycled negative electrodes (Figure 11c,d). These peaks are considerably weaker for prelithiated samples (Figure 11a,b). This indicates that $LiPF_6$ decomposition is minimized in the case of prelithiated samples compared to cycled negative electrodes.

$LiPF_6$ salt is unstable during battery operation resulting in the formation of various species including LiF. Lithium carbonates can also decompose and form LiF upon reaction with HF (from the reaction of $LiPF_6$ and traces of H_2O) and other acidic species.[2]

$$LiPF_6 \rightarrow LiF \downarrow + PF_5 \uparrow \quad (11)$$

$$PF_5 + 2xLi^+ + 2xe^- \rightarrow LiF \downarrow + Li_xPF_{5-x} \downarrow \quad (12)$$

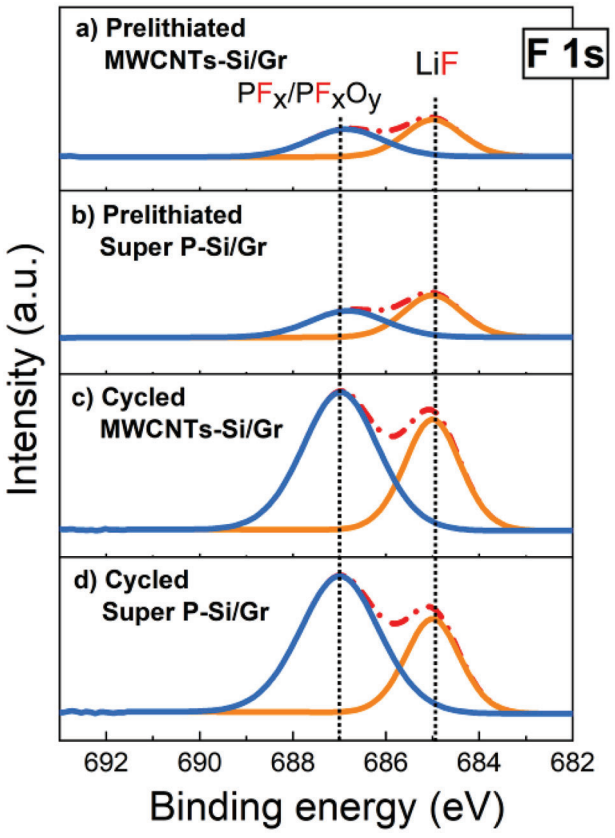

Figure 11. F 1s spectra of a,b) prelithiated and c,d) cycled MWCNTs-Si/Gr and Super P-Si/Gr negative electrodes.

$$PF_5 + H_2O \rightarrow PF_3O \uparrow + 2HF \uparrow \quad (13)$$

$$PF_3O + 2xe^- + 2xLi^+ \rightarrow LiF \downarrow + LiPF_{3-x}O \downarrow \quad (14)$$

$$LiPF_6 + H_2O \rightarrow LiF \downarrow + PF_3O \uparrow + 2HF \uparrow \quad (15)$$

$$2HF + Li_2CO_3 \rightarrow 2LiF \downarrow + H_2O \uparrow + CO_2 \uparrow \quad (16)$$

$$LiPF_6 + Li_2CO_3 \rightarrow 3LiF \downarrow + PF_3O \uparrow + CO_2 \uparrow \quad (17)$$

$$Li_2CO_3 + PF_5 \rightarrow PF_3O \uparrow + LiF \downarrow + CH_3F \uparrow + CO_2 \uparrow \quad (18)$$

The P 2p spectrum (**Figure 12**) presents to be in agreement with the F 1s spectrum that the electrolyte salt degradation is severe with cycled samples. The electrolyte decomposition and thus reaction of organic products take place primarily at higher voltages, while the salt reduction occurs in lower voltage regions. Prelithiation forms first mainly organic components and then the inorganic components until the specific prelithiation dosage is reached.[37]

The Si 2p spectrum (Figure 12) clearly shows that Si is reduced during prelithiation so that products such as Li_xSi and Li_xSiO_y are visible at ≈97 and 101.5 eV. In prelithiated MWCNTs-Si/Gr negative electrode, however, there is an additional peak for Si/Li_xSi at 97 eV, which does not occur in the spectrum of prelithiated Super P-based electrode and in cycled samples, suggesting that the electrode surface is completely covered by organic and inorganic SEI building components on the cycled samples.

Atomic Fraction of SEI Components: **Figure 13** and **Table 4** present the relative atomic fractions of the various SEI-forming components in prelithiated and cycled negative electrodes.

During prelithiation, MWCNTs-Si/Gr negative electrode tends to form higher atomic fractions of lithium carbonate (Li_2CO_3) and lithium alkylcarbonates (RCO_3Li) as compared to Super P-Si/Gr negative electrode (Table 4). This may suggest that more electrolyte is decomposed on MWCNTs due to the high surface area, resulting in enhanced (electro) chemical reactivity. In literature, it has been reported that Li_2CO_3 is an effective and hardly soluble inorganic compound, which plays a crucial role in maintaining the mechanical stability of the SEI layer during cycling, inhibiting further parasitic reactions, thereby enhancing the long-term cycling stability of the battery cells.[37] In contrast, more LiF salt components could be found in the SEI layer on prelithiated and cycled Super P-Si/Gr electrodes, mainly considered as electrochemically, chemically, and mechanically stable products. However, LiF is also endowed with low Li-ion conductivity (Li-ion diffusion energy barrier ≈0.729 eV) compared to lithium alkyl carbonates (≈0.227–0.491 eV).[37] Furthermore, a significant quantity of polymeric (C—O—C) species is identified in the SEI layer of cycled negative electrodes comprising Super P. Polymeric organic compounds exhibit exothermic behavior, thereby contributing to the formation of unstable SEI layer.[39] In summary, it should be emphasized that achieving a stable SEI layer depends on maintaining an appropriate balance between the inorganic and organic components. The development of the SEI layer on the negative electrode based on MWCNTs may demonstrate an ideal composition during both prelithiated and cycled states. **Figure 14** illustrates the SEI layer composition formed on MWCNTs- Si/Gr and Super P- Si/Gr. High atomic fractions of lithium alkyl carbonates are detected in the SEI on MWCNTs-Si/Gr, while the SEI on Super P- Si/Gr includes more inorganic salts such as LiF.

2.5. XPS on Prelithiated–Cycled Negative Electrodes

To further elucidate the impact of in vitro prelithiation on the SEI layer formed on MWCNTs-Si/Gr and Super P-Si/Gr electrodes, XPS was further performed in their prelithiated-cycled states (three times cycled to 0.01 V versus Li/Li^+). **Figure 15** shows the comparative C 1s, O 1s, F1 s, P2 p, Si 2p, and Li 1s spectra of both prelithiated-cycled MWCNTs-Si/Gr and Super P-Si/Gr negative electrodes.

C 1s spectrum of prelithiated-cycled MWCNTs-Si/Gr negative electrode displays a slightly more intense peak at ≈282.2 eV, indicating a higher concentration of lithiated species Li_xC_6/Li_2C_2, possibly due to high surface area and a large amount of defects. It could also imply that the thickness of the SEI layer is slightly thinner in the case of MWCNTs-Si/Gr negative electrodes. This observation is further reinforced by the O 1s spectrum, which shows slightly more intense peak at ≈527.8 eV (attributed to Li_2O) for MWCNT-Si/Gr negative electrode. O 1s spectrum indicates that Super P-Si/Gr negative electrode exhibits a higher concentration of C—O and C═O compounds with slightly intense peaks at ≈532.9 and ≈530.7–531.2 eV, respectively. Moreover, as

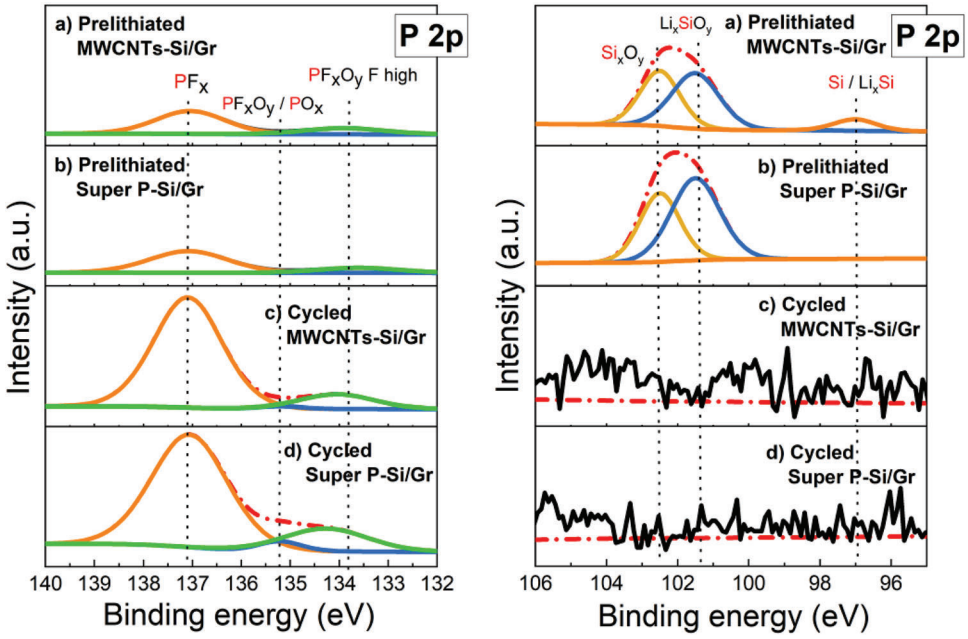

Figure 12. P 2p and Si 2p spectra of: a,b) prelithiated, and c,d) cycled MWCNTs-Si/Gr and Super P-Si/Gr negative electrodes.

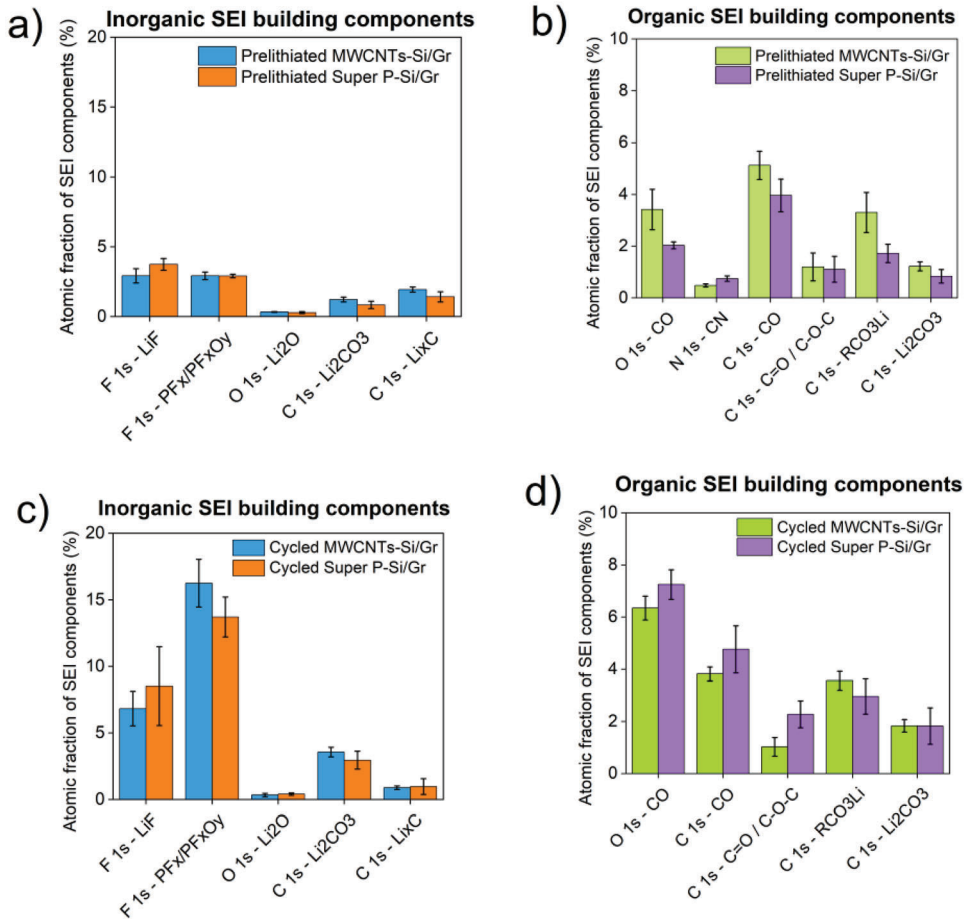

Figure 13. Atomic fractions of organic and inorganic SEI building components formed on prelithiated and cycled MWCNTs-Si/Gr and Super P-Si/Gr negative electrodes.

Table 4. Atomic fractions of organic and inorganic SEI building components of prelithiated and cycled MWCNTs-Si/Gr and Super P-Si/Gr negative electrodes.

State	Sample	Atomic fraction of SEI components [%]					
		LiF	PF_x/PF_xO_y	Li_2CO_3	C—O—C	RCO_3Li	—CN
Prelithiated	MWCNTs-Si/Gr	2.9 ± 0.5	2.9 ± 0.3	1.2 ± 0.2	1.2 ± 0.5	3.3 ± 0.8	0.5 ± 0.1
	Super P-Si/Gr	3.7 ± 0.4	2.9 ± 0.1	0.8 ± 0.3	1.1 ± 0.5	1.7 ± 0.4	0.7 ± 0.1
Cycled	MWCNTs-Si/Gr	6.8 ± 1.3	16.2 ± 1.8	1.8 ± 0.2	1.0 ± 0.4	3.6 ± 0.4	–
	Super P-Si/Gr	8.5 ± 3.0	13.7 ± 1.5	1.8 ± 0.7	2.3 ± 0.5	3.0 ± 0.7	–

can be seen from F1s (≈684.6–684.8 eV) and P2p spectra, higher amounts of inorganic salts such as LiF or phosphate groups like PF_xO_y or PO_x are present in prelithiated-cycled Super P-Si/Gr surface. This could infer that salt degradation is higher in Super P-Si/Gr electrodes; evidencing that the pre-formed SEI layer during the prelithiation stage was not effective. Si 2p spectrum shows an intense peak for Li_xSiO_y compounds with oxidation states of Si^{3+} at ≈102.8 eV - 103.3eV in the prelithiated-cycled Super P-Si/Gr negative electrode. Interestingly, a higher amount of metallic Li can be observed on MWCNTs-Si/Gr negative electrode as shown in the Li 1s spectrum at ≈52.1 e V, which could be attributed to the Li in the SEI building species, and Li trapped in the MWCNTs structure, owing to special features including higher defect density and surface area. This in turn can evidence the presence of a relatively thinner but highly effective SEI layer.

3. Conclusion

Prelithiation conducted on MWCNTs and Super P-containing Si negative electrode-based full-cells has proven to be highly effective method in improving key battery performance indicators including long-term cycling, power output and CE, with more notable positive impact being on MWCNTs-Si/Gr negative electrode-based full-cell compared to its Super P counterpart.- The irreversible capacity during the decisive first cycle is effectively reduced from 62.4 to 25.5 mAh g^{-1} (≈60%) for MWCNTs-Si/Gr and 54.8 mAh g^{-1} to 29.3 mAh g^{-1} (≈47%) for Super P-Si/Gr negative electrodes. Laser microscopy, SEM, RAMAN spectroscopy, ATR-FTIR spectroscopy, and XPS analysis demonstrated significant differences including in the morphology of the electrodes and chemical composition of the SEI layer formed by in vitro prelithiation for both electrode systems. This study proves that combinative use of prelithiation and MWCNTs is critical to boostthe electrochemical performance of Si-rich Si/Gr negative electrodes for high-energy-density LiBs. Results obtained in this study opens a new avenue toward the utilization of MWCNTs- Si rich-based negative electrodes including Si/Gr blends/composites, Si-Oxides (SiO_x), Si-Nitride (SiN_x), etc. in LIBs.

4. Experimental Section

Negative Electrode Preparation: Negative electrodes were produced using Si(Si-alloy, 3 M, 1240 mAh g^{-1} theoretical reversible capacity, Si-alloy content in the range of 51–100 wt%, Gr content in range of 0–49 wt%, 3.3 g cm^{-3} bulk density, particle size distribution in the range of 0.9–24 µm), and Graphite (Gr, Hitachi, 1 g cm^{-3} bulk density, 22.9 µm particle size) as active materials; sodium carboxymethyl cellulose (CMC, Walocel) as water-based binder, Tangled-Multi Walled Carbon Nanotubes (MWCNTs, Graphistrength C100, Arkema) in powder form and Carbon black (Super P, TIMCAL) as electrode conductive additives. MWCNTs material is a solid powder mixture consisting of 75 wt% of MWCNTs and 25 wt% of CMC (> 90% carbon purity, 0.05–0.15 g cm^{-3} of bulk density, number of intrinsic layers 5–15, outer diameter ranges 10–15 nm, length in the range of 0.1–10 µm, 0.2–0.5 mm agglomerate size, 175 m^2 g^{-1} of specific surface area).[18] The reference conductive additive material exhibits a surface area of 62 m^2 g^{-1} (provided by the supplier).

For negative electrode fabrication, the slurries were prepared by mixing the components in small cups (60 mL) with a planetary micro mill (pulverisette 7, Fritsch). All ingredients were previously dry-mixed at 800 rpm for 10 min and further mixed at the same speed for 1 h by adding distilled water to form a slurry. Table 1 shows the negative electrode composition

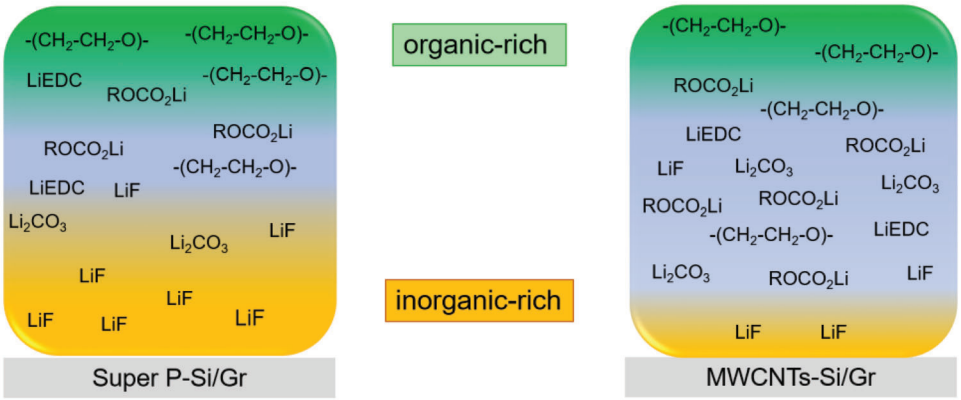

Figure 14. Illustration of SEI layer composition formed on prelithiated MWCNTs-Si/Gr and Super P-Si/Gr negative electrodes.

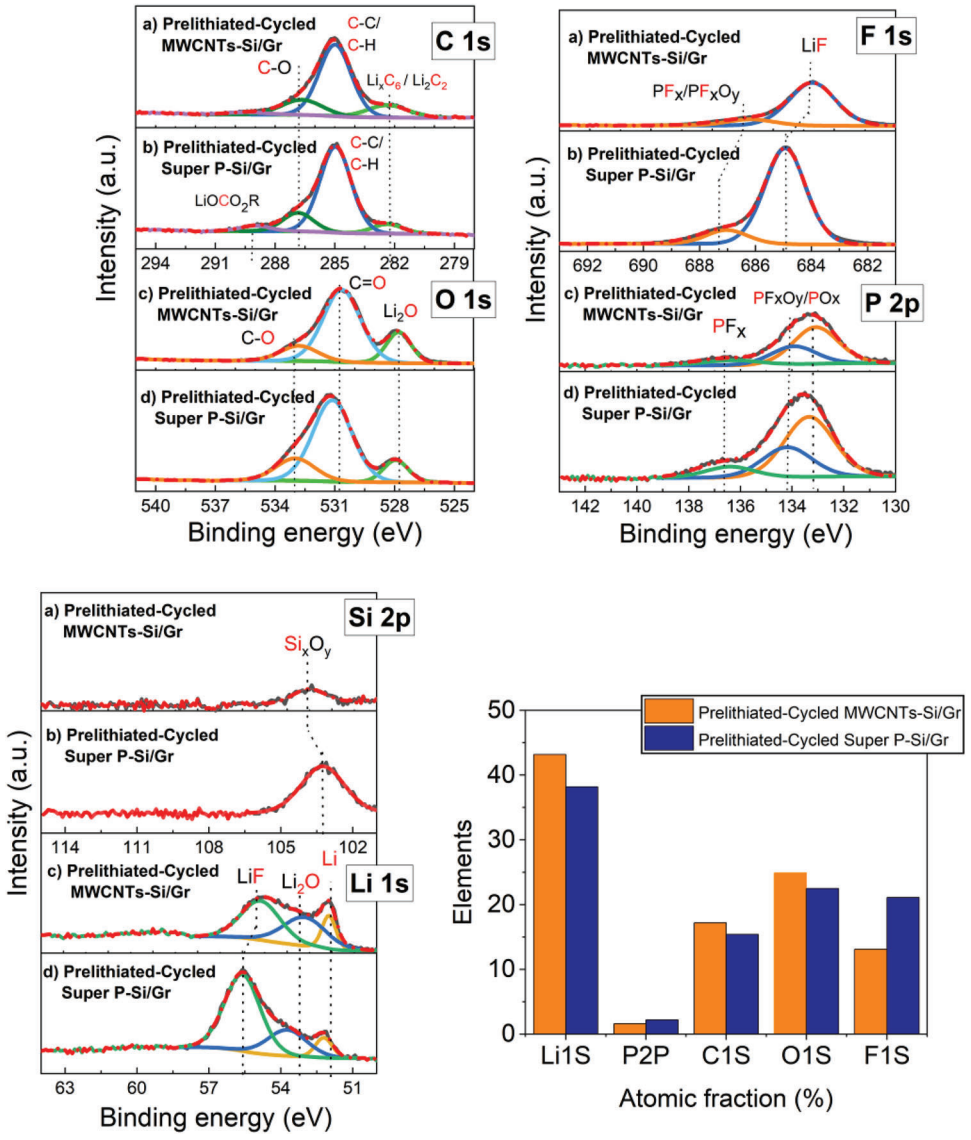

Figure 15. Comparative C 1s, O 1s, F1 s, P2 p, Si 2p, and Li 1s spectra of both prelithiated-cycled MWCNTs-Si/Gr and Super P-Si/Gr negative electrodes. Atomic fractions (%) of elements for prelithiated-cycled and pristine-cycled MWCNTs-Si/Gr and Super P-Si/Gr negative electrodes.

in weight percentage (wt%). After the mixing, the slurries were coated on 14 µm thick ED copper foil (Cu, CustomCells) with a coating unit (CUF 5, SUMET, Germany). The coatings were dried for 24 h at Room Temperature (RT), afterwards calendered at 10 Nm mm^{-1} pressure (SUMET, Germany), and punched with a 16 mm high precision electrode cutter (EL-CELL) for coin-cell building. Punched electrodes were dried overnight at 80 °C in a vacuum oven (Buechi, Glass oven B-585 Drying).

Surface Chemistry Characterization: Laser microscopy analysis (Keyence VK-9700 magnification up to 3600) was conducted on samples that were placed in a glovebox with an argon atmosphere (O_2 < 1 ppm, H_2O < 0.5 ppm). SEM was performed on the same electrodes using a Zeiss Supra 55 system to characterize the sample morphologies withan accelerating voltage of 5 or 10 kV. Raman spectra were acquired using a Bruker Senterra spectrometer equipped with a 532 nm He–Ne laser. The micro-Raman measurements were carried out with a 50× magnification objective under dry room conditions (Dew point ←55 °C, Room Temperature = 20°C). For every spectrum, 25 points, arranged in a square and having a distance of 5 µm from each other, were measured. The average was then calculated and used as a representative measure of a 25 μm^2 Surface. The spectra were baseline corrected and noise reduced. ATR-FTIR measurements were performed by Bruker Senterra spectrometer (Vertex 70) in attenuated total reflection (ATR) mode in dry room conditions (Dew point ←55 °C, Room Temperature = 20°C) in the range of 4000–500 cm^{-1}. The spectra were acquired at a resolution of 4 cm^{-1} for 256 scans. Prior to the characterization measurements, the pristine samples were dried overnight (20 h) at 80 °C under vacuum (Buechi, Glass oven B-585 Drying, Germany). For sensitive samples (i.e., prelithiated and cycled), cells were disassembled in the glovebox with an argon atmosphere (O_2 < 1 ppm, H_2O < 0.5 ppm) and dried for 1 h under vacuum. The electrodes were then sealed in an aluminum pouch bag and transferred to the dry room. Following, measurement was carried out immediately after opening the pouch bag. To further investigate the surface chemistry of prelithiated, pristine-cycled, and prelithiated-cycled samples, XPS was performed with an Axis Ultra DLD (Kratos Analytical Ltd) using monochromatic Al K_α X-Rays ($h\nu$ = 1486 eV, 12 kV, 10 mA) and a charge neutralizer for compensation of surface charging. For core

level spectra, a pass energy of 20 eV and a step width of 0.1 eV were applied at a 0°angle of emission to the surface normal. Spectra were recorded from three measurement positions to ensure reproducibility.

Electrochemical Prelithiation: In this study, electrochemical prelithiation was selected due to its controllability and scalability.[40] Negative electrodes were prelithiated in vitro (prior to the assembly of the full cell) within the half coin cell (CR2032) configuration. Chevrier et. cal. suggested the implementation of a Li reservoir (prelithiation dosage) ranging from 10% to 20%. This approach offers the advantage of achieving both a higher energy density and an extended cycle life.[7] and a prelithiation degree of 20% was accordingly selected in this study.

The process was adjusted in coin-cell format using Li metal (15.8 mm) as counter electrode and 90 µL of electrolyte of 1.2 M $LiPF_6$ in ethylene carbonate (EC) /ethyl methyl carbonate (EMC) (3/7) + 10 wt% fluoroethylene carbonate (FEC) (E-lyte). Coin cells were built in an argon-filled glove box (O_2 < 1 ppm, H_2O < 0.5 ppm). As prelithiation dosage, as mentioned above, ≈20% was optimized and thus selected, and was obtained from the first discharge capacity (1st lithiation) of half-cells. After prelithiation, coin cells were disassembled in the argon-filled glove box and the negative electrodes were recovered and rinsed in 1 M THF (tetrahydrofuran, Sigma Aldrich) with 10 wt% of TEOSCN (3-(Triethoxysilyl) propionitrile, Sigma Aldrich, ≈97% purity) solution. The remaining prelithiated negative electrodes were dried for 1 h under a vacuum. Details of the experimental procedure is also given in our previous work.[41]

Full-cell Assembly and Electrochemical Performance Tests: Full-cells were constructed by coupling pristine and prelithiated negative electrodes with NMC622 (16 mg cm^{-2}) positive electrode using glass fiber GF/C Watman (ϕ = 17 mm) as separator and 90 µL of electrolyte 1.2 M $LiPF_6$ in EC/EMC (3/7) + 10 wt% FEC as electrolyte solution. Electrochemical testing of the full-cell was performed by Neware BTS4000-5V10mA in the voltage window of 2.8–4.35 V with two times formation process at C/20 CC charge and CC discharge. After formation, the cells were cycled at C/2 with CC charge and CC discharge mode. The negative/positive ratio (N/P) was between 1.2–1.3. The rate capability of full cells was measured at different C-rates, ranging from 0.1 C to 1 C.

Acknowledgements

This research was funded by the Federal Ministry of Education and Research of Germany (BMBF) for the projects PräLi (03XP0238X) and ProMIZ (13XP0397B).

Open access funding enabled and organized by Projekt DEAL.

Conflict of Interest

The authors declare no conflict of interest.

Data Availability Statement

The data that support the findings of this study are available from the corresponding author upon reasonable request.

Keywords

carbon nanotubes, lithium-ion battery, prelithiation, silicon/graphite anode, solid electrolyte interphase (SEI)

Received: February 23, 2024
Revised: April 26, 2024
Published online: June 8, 2024

[1] a) T. Horiba, *Proceed. IEEE* **2014**, *102*, 939; b) A. Yoshino, in *Lithium-ion batteries*, Elsevier, Amsterdam **2014**, pp. 1–20; c) Y. Nishi, *The Electrochemical Society Interface* **2016**, *25*, 71; d) C. J. Murray, *IEEE Spectrum* **2023**, *60*, 40; e) F. Schomburg, B. Heidrich, S. Wennemar, R. Drees, T. Roth, M. Kurrat, H. Heimes, A. Jossen, M. Winter, J. Y. Cheong, *Energy & Environmental Science* **2024**, *17*, 2686.

[2] a) G. Gebresilassie Eshetu, M. Armand, B. Scrosati, S. Passerini, *Angew. Chem.* **2014**, *126*, 13558; b) A. Shukla, T. P. Kumar, *ACS Publications* **2013**, *4*, 551; c) M. Winter, B. Barnett, K. Xu, *Chem. Rev.* **2018**, *118*, 11433; d) H. J. Kim, S. Choi, S. J. Lee, M. W. Seo, J. G. Lee, E. Deniz, Y. J. Lee, E. K. Kim, J. W. Choi, *Nano Lett.* **2016**, *16*, 282; e) G. G. Eshetu, T. Diemant, S. Grugeon, R. J. Behm, S. Laruelle, M. Armand, S. Passerini, *ACS Appl. Mater. Interfaces* **2016**, *8*, 16087; f) G. G. Eshetu, E. Figgemeier, *ChemSusChem* **2019**, *12*, 2515.

[3] M. Kabir, D. E. Demirocak, *Int. J. Energy Res.* **2017**, *41*, 1963.

[4] H. Shi, J. Barker, M. Saidi, R. Koksbang, *J. Electrochem. Soc.* **1996**, *143*, 3466.

[5] a) W. Zhao, C. Zhao, H. Wu, L. Li, C. Zhang, *J. Energy Storage* **2024**, *81*, 110409; b) Y. Liu, H. Shi, Z. S. Wu, *Energy Environ. Sci.* **2023**, *16*, 4834; c) X. Ding, Q. Zhou, X. Li, X. Xiong, *Chem. Commun.* **2024**, *60*, 2472.

[6] a) G. G. Eshetu, H. Zhang, X. Judez, H. Adenusi, M. Armand, S. Passerini, E. Figgemeier, *Nat. Commun.* **2021**, *12*, 5459; b) S. N. D. Surabhi, C. Shah, V. Mandala, P. Shah,

[7] a) F. Aupperle, N. von Aspern, D. Berghus, F. Weber, G. G. Eshetu, M. Winter, E. Figgemeier, *ACS Appl. Energy Mater.* **2019**, *2*, 6513; b) V. L. Chevrier, L. Liu, R. Wohl, A. Chandrasoma, J. A. Vega, K. W. Eberman, P. Stegmaier, E. Figgemeier, *J. Electrochem. Soc.* **2018**, *165*, A1129; c) V. L. Chevrier, L. Liu, D. B. Le, J. Lund, B. Molla, K. Reimer, L. J. Krause, L. D. Jensen, E. Figgemeier, K. W. Eberman, *J. Electrochem. Soc.* **2014**, *161*, A783; d) M. Marinaro, D.-h. Yoon, G. Gabrielli, P. Stegmaier, E. Figgemeier, P. C. Spurk, D. Nelis, G. Schmidt, J. Chauveau, P. Axmann, *J. Power Sources* **2017**, *357*, 188.

[8] a) Y. Jin, B. Zhu, Z. Lu, N. Liu, J. Zhu, *Adv. Energy Mater.* **2017**, *7*, 1700715; b) Y. Zhao, X. Pan, M. Liu, X. Chen, R. Zhang, X. Zhiyong, *RSC Adv.* **2023**, *13*, 35026.

[9] T.-w. Kwon, J. W. Choi, A. Coskun, *Chem. Soc. Rev.* **2018**, *47*, 2145.

[10] a) F. H. Du, K. X. Wang, J. S. Chen, *J. Mater. Chem. A* **2016**, *4*, 32; b) E. Pollak, G. Salitra, V. Baranchugov, D. Aurbach, *J. Phys. Chem. C* **2007**, *111*, 11437; c) M. Pharr, K. Zhao, X. Wang, Z. Suo, J. J. Vlassak, *Nano Lett.* **2012**, *12*, 5039.

[11] a) L. Li, C. Fang, G. He, Y. Huang, *ACS Appl. Mater. Interfaces* **2023**, *15*, 36344; b) L. Köbbing, A. Latz, B. Horstmann, *Adv. Funct. Mater.* **2024**, *34*, 2308818.

[12] G. F. I. Toki, M. K. Hossain, W. U. Rehman, R. Z. A. Manj, L. Wang, J. Yang, *Industr. Chem. Mater.* **2024**, *2*, 226.

[13] a) X. Fan, T. Cai, S. Wang, Z. Yang, W. Zhang, *Small* **2023**, *19*, 2300431; b) T. Kim, Y. Mo, K. Nahm, S. M. Oh, *J. Power Sources* **2006**, *162*, 1275; c) S. Huang, J. Yao, X. Li, H. Liu, Y. Qin, X. Wang, D. Luo, L. Shui, *APL Mater.* **2024**, *12*, 011126.

[14] a) X. Li, F. Kang, X. Bai, W. Shen, *Electrochem. Commun.* **2007**, *9*, 663; b) Q. Zhang, Z. Yu, P. Du, C. Su, *Recent Pat. Nanotechnol.* **2010**, *4*, 100; c) S. Fang, L. Shen, X. Zhang, in *Industrial applications of carbon nanotubes*, Elsevier, Amsterdam **2017**, pp. 251–276; d) P. Sehrawat, C. Julien, S. Islam, *Mater. Sci. Eng., B* **2016**, *213*, 12; e) X. Yan, Z. Fu, L. Zhou, L. Hu, Y. Xia, W. Zhang, Y. Gan, J. Zhang, X. He, H. Huang, *ACS Appl. Mater. Interfaces* **2023**, *15*, 17986.

[15] a) J. Zhao, Z. Lu, H. Wang, W. Liu, H. W. Lee, K. Yan, D. Zhuo, D. Lin, N. Liu, Y. Cui, *J. Am. Chem. Soc.* **2015**, *137*, 8372; b) X. M. Liu, Z. Dong Huang, S. Woon Oh, B. Zhang, P. C. Ma, M. M. Yuen, J. K. Kim, *Compos. Sci. Technol.* **2012**, *72*, 121.

[16] X. Liu, Z. Wu, L. Xie, L. Sheng, J. Liu, L. Wang, K. Wu, X. He, *Energ. Environm. Mater.* **2023**, *6*, e12501.

[17] a) R. I. Rubel, M. H. Ali, M. A. Jafor, M. M. Alam, *AIMS Mater. Sci.* **2019**, *6*, 756; b) X. Jia, F. Wei, in *Single-Walled Carbon Nanotubes*,

Topics in Current Chemistry Collections, (Eds: Y. Li, S. Maruyama), Springer, Cham **2019**, Ch. 11.
[18] Y. Dall'Agnese, Doctoral-Thesis, Université Paul Sabatier - Toulouse III 2016Y., Université Paul Sabatier – Toulouse III **2016**.
[19] F. Holtstiege, A. Wilken, M. Winter, T. Placke, *Phys. Chem. Chem. Phys.* **2017**, *19*, 25905.
[20] a) R. Jung, M. Metzger, D. Haering, S. Solchenbach, C. Marino, N. Tsiouvaras, C. Stinner, H. A. Gasteiger, *J. Electrochem. Soc.* **2016**, *163*, A1705; b) M. Wetjen, D. Pritzl, R. Jung, S. Solchenbach, R. Ghadimi, H. A. Gasteiger, *J. Electrochem. Soc.* **2017**, *164*, A2840; c) N. Hamzelui, G. G. Eshetu, E. Figgemeier, *J. Energy Storage* **2021**, *35*, 102098.
[21] A. Rezqita, A. R. Kathribail, J. Kahr, M. Jahn, *J. Electrochem. Soc.* **2019**, *166*, A5483.
[22] X. L. Wang, K. An, L. Cai, Z. Feng, S. E. Nagler, C. Daniel, K. J. Rhodes, A. D. Stoica, H. D. Skorpenske, C. Liang, *Sci. Rep.* **2012**, *2*, 747.
[23] a) L. A. Bokobza, J. Zhang, *eXPRESS Polym. Lett.* **2012**, *6*, 601; b) M. S. Dresselhaus, A. Jorio, M. Hofmann, G. Dresselhaus, R. Saito, *Nano Lett.* **2010**, *10*, 751.
[24] E. Markervich, G. Salitra, M. D. Levi, D. Aurbach, *J. Power Sources* **2005**, *146*, 146.
[25] a) H. Murphy, P. Papakonstantinou, T. T. Okpalugo, *J. Vac. Sci. Technol., B: Nanotechnol. Microelectron.: Mater., Process., Meas., Phenom.* **2006**, *24*, 715; b) Y. C. Choi, K. I. Min, M. S. Jeong, *J. Nanomater.* **2013**, *2013*, 2; c) Y. A. Kim, M. Kojima, H. Muramatsu, D. Shimamoto, T. Hayashi, M. Endo, M. Terrones, M. S. Dresselhaus, *J. Raman Spectrosc.* **2008**, *39*, 1183.
[26] A. C. Ferrari, J. Robertson, *Phys. Rev. B* **2000**, *61*, 14095.
[27] A. Kaniyoor, S. Ramaprabhu, *AIP Advances* **2012**, *2*, 032183.
[28] a) J. Hu, Z. Xu, X. Li, S. Liang, Y. Chen, L. Lyu, H. Yao, Z. Lu, L. Zhou, *J. Power Sources* **2020**, *462*, 228098; b) J. Niu, R. Shao, M. Liu, J. Liang, Z. Zhang, M. Dou, Y. Huang, F. Wang, *Energy Storage Mater.* **2018**, *12*, 145.
[29] a) R. Schmitz, R. A. Mueller, R. W. Schmitz, C. Schreiner, M. Kunze, A. Lex-Balducci, S. Passerini, M. Winter, *J. Power Sources* **2013**, *233*, 110; b) M.-T. F. Rodrigues, V. A. Maroni, D. J. Gosztola, K. P. Yao, K. Kalaga, I. A. Shkrob, D. P. Abraham, *ACS Appl. Energy Mater.* **2018**, *2*, 873; c) A. Krause, O. Tkacheva, A. Omar, U. Langklotz, L. Giebeler, S. Dörfler, F. Fauth, T. Mikolajick, W. M. Weber, *J. Electrochem. Soc.* **2019**, *166*, A5378; d) V. Eshkenazi, E. Peled, L. Burstein, D. Golodnitsky, *Solid State Ionics* **2004**, *170*, 83; e) Y. Xiang, M. Tao, X. Chen, P. Shan, D. Zhao, J. Wu, M. Lin, X. Liu, H. He, W. Zhao, *Nat. Commun.* **2023**, *14*, 177.
[30] G. G. Eshetu, S. Grugeon, G. Gachot, D. Mathiron, M. Armand, S. Laruelle, *Electrochim. Acta* **2013**, *102*, 133.
[31] a) D. Aurbach, M. D. Levi, E. Levi, A. Schechter, *J. Phys. Chem. B* **1997**, *101*, 2195; b) D. Aurbach, B. Markovsky, A. Shechter, Y. Ein-Eli, H. Cohen, *J. Electrochem. Soc.* **1996**, *143*, 3809; c) D. Aurbach, Y. Ein-Ely, A. Zaban, *J. Electrochem. Soc.* **1994**, *141*, L1; d) D. Aurbach, Y. Gofer, M. Ben-Zion, P. Aped, *J. Electroanal. Chem.* **1992**, *339*, 451; e) D. Aurbach, Y. Gofer, J. Langzam, *J. Electrochem. Soc.* **1989**, *136*, 3198.
[32] Y. H. T. Tran, J. Han, S. W. Song, *J. Electrochem. Soc.* **2021**, *168*, 020529.
[33] R. Marom, O. Haik, D. Aurbach, I. C. Halalay, *J. Electrochem. Soc.* **2010**, *157*, A972.
[34] a) L. Huang, Z. Min, Q. Zhang, *Rev. Adv. Mater. Sci* **2014**, *36*, 13; b) P. Verma, P. Maire, P. Novák, *Electrochim. Acta* **2010**, *55*, 6332.
[35] G. V. Zhuang, P. N. Ross, *Electrochem. Solid-State Lett.* **2003**, *6*, A136.
[36] a) S. P. Kim, A. C. Van Duin, V. B. Shenoy, *J. Power Sources* **2011**, *196*, 8590; b) G. V. Zhuang, K. Xu, H. Yang, T. R. Jow, P. N. Ross, *J. Phys. Chem. B* **2005**, *109*, 17567.
[37] S. J. An, J. Li, C. Daniel, D. Mohanty, S. Nagpure, D. L. Wood, III, *Carbon* **2016**, *105*, 52.
[38] a) R. Dedryvère, L. Gireaud, S. Grugeon, S. Laruelle, J. M. Tarascon, D. Gonbeau, *J. Phys. Chem. B* **2005**, *109*, 15868; b) J. Zheng, P. Yan, D. Mei, M. H. Engelhard, S. S. Cartmell, B. J. Polzin, C. Wang, J. G. Zhang, W. Xu, *Adv. Energy Mater.* **2016**, *6*, 1502151.
[39] J. O. Besenhard, M. Winter, *Pure Appl. Chem.* **1998**, *70*, 603.
[40] F. Li, Y. Cao, W. Wu, G. Wang, D. Qu, *Small Methods* **2022**, *6*, 2200411.
[41] L. Ünal, V. Maccio-Figgemeier, G. Gebresilassie Eshetu, E. Figgemeier, *ChemElectroChem. Portico* **2024**, https://doi.org/10.1002/celc.202400146.